



ELSEVIER

International Journal of Solids and Structures 41 (2004) 481–509

INTERNATIONAL JOURNAL OF  
**SOLIDS and**  
**STRUCTURES**

[www.elsevier.com/locate/ijsolstr](http://www.elsevier.com/locate/ijsolstr)

# On predicting the effective elastic properties of polymer bonded explosives using the recursive cell method

Biswajit Banerjee <sup>\*</sup>, Daniel O. Adams

Department of Mechanical Engineering, University of Utah, 50 S Central Campus Drive, 2120 MEB, Salt Lake City, UT 84112, USA

Received 22 December 2002; received in revised form 8 September 2003

---

## Abstract

Polymer bonded explosives are particulate composites containing elastic particles in a viscoelastic binder. The particles occupy an extremely high fraction of the volume, often greater than 90%. Under low strain rate loading ( $\sim 0.001\text{--}1\text{ s}^{-1}$ ) and at room temperature and higher, the elastic modulus of the particles can be four orders of magnitude higher than that of the binder. Rigorous bounds and analytical estimates for the effective elastic properties of these materials have been found to be inaccurate. The computational expense of detailed numerical simulations for the determination of effective properties of these composites has led to the search for a faster technique. In this work, one such technique based on a real-space renormalization group approach is explored as an alternative to direct numerical simulations in determining the effective elastic properties of PBX 9501. The method is named the recursive cell method (RCM). The differential effective medium approximation, the finite element method, and the generalized method of cells (GMC) are investigated with regard to their suitability as homogenizers in the RCM. Results show that the RCM overestimates the effective properties of particulate composites and PBX 9501 unless large blocks of subcells are renormalized and the particles in a representative volume element are randomly distributed. The GMC homogenizer is found to provide better estimates of effective elastic properties than the finite element based homogenizer for composites with particle volume fractions less than 0.80.

© 2003 Elsevier Ltd. All rights reserved.

**Keywords:** Particulate composites; Elastic properties; Renormalization; Generalized method of cells; Finite elements

---

## 1. Introduction

One of the goals of multi-scale modeling of materials is to predict the behavior of these materials across many different length scales. These length scales range from the atomistic (nanometers) to the macroscopic (meters). Many multi-scale simulations move from a smaller scale to a larger one by using coarse-grained representations of the material and its microstructure in the larger scale. Micromechanics provides a process by which coarse-graining can be achieved by producing effective properties that can be used in the macroscopic simulations.

---

<sup>\*</sup> Corresponding author. Tel.: +1-801-585-5239; fax: +1-801-585-9826.

E-mail address: [banerjee@eng.utah.edu](mailto:banerjee@eng.utah.edu) (B. Banerjee).

For two-phase random composite materials with relatively low volume fractions of the dispersed phase (<0.50), excellent estimates of the effective elastic properties can be obtained from micromechanics-based rigorous bounds or analytical approximations. However, such estimates are grossly inaccurate for particulate composites containing extremely high volume fractions of particles and strong modulus contrasts between the phases. This is especially true for polymer bonded explosives (PBXs) which can have particle volume fractions greater than 0.90 and modulus contrasts between particles and binder greater than 20,000. For PBX 9501, third-order upper and lower bounds on effective moduli can be three orders of magnitude apart and analytical estimates can be an order of magnitude different from experimental values.

In the absence of close bounds and accurate analytical approximations (Banerjee and Adams, in press), the prediction of effective properties of PBXs requires numerical simulations that explicitly consider the microstructure of the composite. However, direct numerical simulations are computationally expensive. Such simulations become prohibitive when the effective properties of the composite are to be computed in the course of a multi-scale simulation.

Methods derived from the real-space renormalization group (RSRG) (Wilson, 1971a, 1979) have been found to provide an accurate means of determining certain effective properties of materials (such as conductivity, permeability, etc.) with relatively low computational cost. The recursive cell method (RCM) attempts to apply the idea of renormalization to the determination effective elastic properties of high volume fraction and high modulus contrast particulate composites such as PBXs.

The idea behind renormalization is that, in a large system, local high frequency oscillations of a state variable do not influence the low frequency behavior of the system. Thus, if a method can be found that accurately averages out the local fluctuations, then a larger system can be built with the averaged local regions as the building blocks. This idea is implemented in the RCM by dividing the representative volume element (RVE) into subcells using a regular grid. Small blocks of subcells are then homogenized in a recursive manner until an effective property of the composite is obtained. The homogenization of blocks of subcells is performed using finite elements, the generalized method of cells (GMC) or any other suitable technique. For simplicity, only two phase particulate composites are considered in this work. However, the number of phases is not limited in any way by the method.

The organization of this paper is as follows. Section 2 discusses the rationale behind using RSRG approaches for high volume fraction particulate composites. The RCM is described in Section 3 and homogenization techniques appropriate to this method are presented. Section 4 provides background information on PBXs and PBX 9501, bounds and analytical estimates of the effective properties of PBX 9501, followed by a brief discussion of the difficulties associated with direct finite element and generalized method of cells analyses of PBX microstructures. Predictions from the RCM using different homogenizers are discussed in Section 5. Finally, the results are summarized and conclusions presented in Section 6.

## 2. Renormalization

The original use of the renormalization group (RG) occurs in quantum electrodynamics (Stueckelberg and Petermann, 1953; Gell-Mann and Low, 1954; Wilson, 1971a,b). The goal in that context was to replace the fine structure of point masses and charges with observable quantities. The RG is a group  $\mathcal{G}(\mathbf{T}_s)$  of transformations  $\mathbf{T}_s$  that take a point  $x_n \in \mathbb{R}^+$  into the point  $x_{n+1} \in \mathbb{R}^+$  (in one dimension) in such a way that

$$x_{n+1} = x_n f(C_{n+1}/C_n, x_n) \equiv x_n f(s, x_n), \quad (1)$$

where  $C_n, C_{n+1}$  are constants that couple the two points,  $f$  is a function of  $s$  and  $x_n$ . Then, the transformation  $\mathbf{T}$  has the group property  $\mathbf{T}_{s2} = \mathbf{T}_{s1}\mathbf{T}_s$  if  $s_2 = s_1 s$ . The identity transformation  $\mathbf{T}_1$  exists, as does the

transformation inverse  $\mathbf{T}_s^{-1}$ . The transformation is usually nonlinear, unlike the deformation gradient tensor in finite elasticity.

The RSRG was originally proposed by Kadanoff (Wilson, 1971a). The idea of RSRG methods is to consider a material to be divided into blocks containing  $N^3$  cells (or lattice sites). Each block of material is then considered to act as a unit (a single effective material) in a new, scaled lattice. The new set of cells (or lattice sites) are again divided into blocks and subjected to the same process until a fixed point is obtained. The fixed point is that situation in which each block has the same material properties. If we consider a lattice model of an elastic solid, the RSRG approach consists of a set of transformations  $\mathbf{T} \subset \mathbf{T}_s$  that take a lattice of spacing  $l$  with probability density  $P_n(K, \mu)$  into another lattice of spacing  $\alpha l$  with probability density

$$P_{n+1}(K, \mu) = \mathbf{T}(P_n(K, \mu)), \quad (2)$$

where  $K$  is the bulk modulus,  $\mu$  is the shear modulus,  $P_{n+1}$  is the probability distribution of elastic properties on the new lattice, and  $P_n$  is the probability distribution on the old lattice.

The probability distributions  $P$  and the transformation  $T$  are usually not amenable to analytical representation. Hence, an approximate method is usually used to determine the discrete distribution of properties on the lattice at each recursion. The RVE that is homogenized using this approach is assumed to be considerably larger than the size of individual subcells. Therefore, scale similarity arguments can be used to justify the use of a RSRG approach if the RVE is infinite compared to each subcell. In numerical RSRG approaches, an infinitely sized RVE is not possible to simulate. Instead a finite sized RVE is chosen and scale similarity is assumed to exist in that RVE. A complete review of numerical RSRG approaches is outside the scope of this work. However, we will try to motivate and explore the applicability of one such approach to PBX materials.

Standard homogenization theories average all the fluctuations in the RVE in a single step usually using a perturbation-based approach. Such effective medium theories lead to unreasonable effective properties when the fluctuations are large and rapid, as is the case in high modulus contrast/high volume fraction particulate composites (Banerjee and Adams, in press).

In contrast, RSRG approaches smooth out the local fluctuations at each step ( $n + 1$ ) of the recursion after a detailed computation at the initial step ( $n_1$ ). The physical argument that is used to justify this approach is that local fluctuations in the properties do not propagate their effects to the long range. This argument requires that length scales in the problem are well separated.

Renormalization-based techniques have been widely used for studying critical phenomena in percolating systems (Feng and Sahimi, 1985; Stauffer and Aharony, 1992) including elastic networks (Feng and Sahimi, 1985). Other applications to percolating systems include the calculation of the effective conductance of lattices (Bernaconi, 1978) and composites (Shah and Ottino, 1986), the effective permeability of rocks (King, 1989), effective dispersivities of flows (Jaekel and Vereecken, 1997), the effective hydraulic conductivity of heterogeneous media (Hristopulos and Christakos, 1999; Renard et al., 2000), and the effective elastic properties of porous media (Pouyet et al., 1996).

The similarity of PBXs to percolating systems is that stress is transported mainly (but not exclusively) through contact between particles (Bardenhagen et al., 2001), in a manner analogous to percolation through the material. If the RVE is large enough, the local length scales are well separated from macroscopic scales. This consideration has motivated the use of a RSRG method to estimate the effective properties of PBXs. An additional incentive is that RSRG methods are considerably faster than conventional numerical averaging methods because the whole domain is not homogenized at a time. Instead, some averaging is done at a smaller length scale and the average properties are appropriately scaled for use at a larger length scale.

Further support for the percolation analogy is provided in Fig. 1(a). The figure shows the variation of the effective two-dimensional bulk modulus with particle volume fraction. The data have been computed

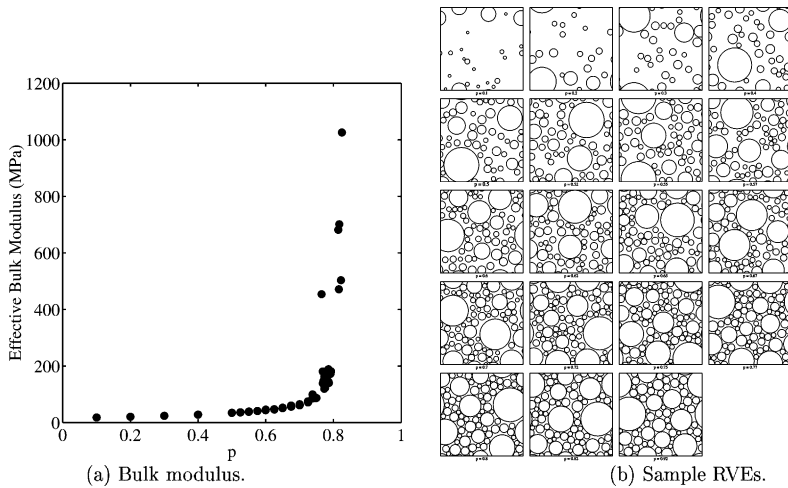


Fig. 1. Effective two-dimensional bulk modulus vs. volume fraction ( $p$ ) for particulate composites with a modulus contrast of 25,000.

using detailed finite element analyses of square RVEs containing circular particles in a continuous binder. The particle size distribution is based on that of the dry blend of PBX 9501 (Skidmore et al., 1997). More information of PBX 9501 is given in Section 4.

The Young's modulus of the particles is 25,000 MPa while that of the binder is 1 MPa. The Poisson's ratio of the particles is 0.20 and that of the binder is 0.49. The bulk moduli are approximately 14,000 MPa for the particles and 2 MPa for the binder. The finite element homogenization approach and its convergence behavior have been described in detail elsewhere (Banerjee et al., 2003). A brief description in the context of the RCM is provided in Section 3.2. All material properties used as inputs to the models in what follows are three-dimensional properties. Also, all comparisons are made between three-dimensional properties.

Ninety-four randomly generated microstructures (similar to those shown in Fig. 1(b)) have been used to calculate the effective bulk moduli shown in Fig. 1(a). From the figure, it can be observed that the percolation threshold is around 0.80 for such composites. PBXs with volume fractions  $>0.90$  lie near this threshold. This suggests that the transport of stress through PBXs is analogous to transport through percolating networks and similar techniques may be used to study the features of both PBXs and percolating networks.

### 3. The recursive cell method

A schematic of the RCM is shown in Fig. 2. The RCM approach requires the RVE to be initially discretized into a regular grid of subcells. The subcells are assigned material properties depending on the particle distribution in the RVE. The subcells in the original grid are grouped into blocks of  $N \times N$  subcells. The effective elastic properties of each block are calculated using an approximate homogenization technique, e.g., using an effective medium approximation, a lattice spring model, the finite element method, the generalized method of cells or combinations of these methods. These stiffnesses are then assigned to a new, coarser grid.

In standard renormalization approaches, the above process is repeated until a "fixed point" is reached where the effective properties of all the blocks have the same value. However, in the simulations performed

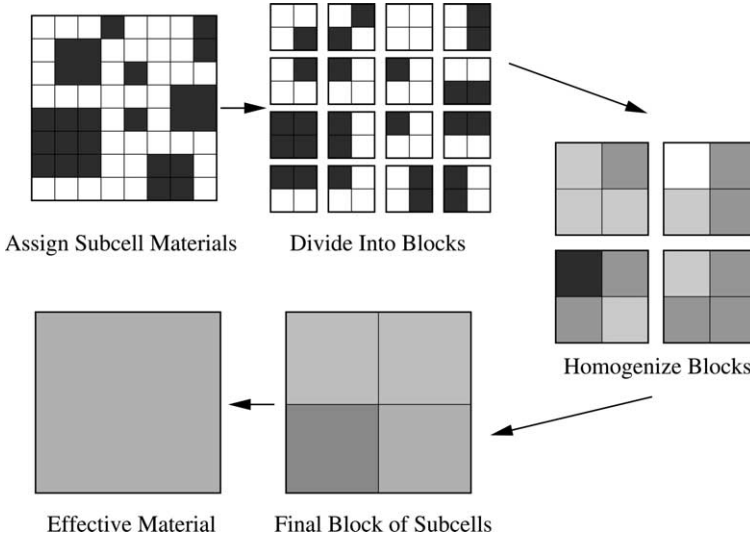


Fig. 2. Schematic of the recursive cell method.

in this work, the recursion terminates when only one homogeneous block remains after a fixed number of iterations since the domain is finite. The properties of this homogeneous block are assumed to be the effective properties of the RVE. For simplicity, only two-dimensional models of particulate composites and PBX 9501 are considered in this paper. Extension of RCM to three-dimensions follows the same procedure and is straightforward.

### 3.1. Differential effective medium homogenization

In this section, we discuss how a differential effective medium theory (D-EMT) can be used to homogenize a block in RCM. The usual D-EMT (Markov, 2000; Garbozci and Berryman, 2001 and references therein) procedure is as follows. Suppose particles with elastic moduli  $K_p$  and  $\mu_p$  are embedded in a binder with elastic moduli  $K_b$  and  $\mu_b$ . Suppose that a dilute volume fraction  $p$  of particles have been placed in the binder. The effective moduli  $K_{\text{eff}}$  and  $\mu_{\text{eff}}$  of the resulting composite are computed using the dilute approximation. The resulting composite is treated as a homogeneous material with moduli equal to the computed moduli. Suppose then that more particles are added by removing a differential volume ( $dV$ ) from the composite, and replacing it with an equivalent volume of particles. The new composite properties can again be calculated using the dilute limit. As  $dV \rightarrow 0$ , the process can be approximated by the following coupled differential equations for the effective elastic moduli,

$$(1-p) \frac{dK_{\text{eff}}}{dp} = (K_p - K_{\text{eff}}) \left( \frac{K_{\text{eff}} + 4/3\mu_{\text{eff}}}{K_p + 4/3\mu_{\text{eff}}} \right), \quad (3)$$

$$(1-p) \frac{d\mu_{\text{eff}}}{dp} = (\mu_p - \mu_{\text{eff}}) \left( \frac{\mu_{\text{eff}} + \varphi_{\text{eff}}}{K_p + \varphi_{\text{eff}}} \right), \quad (4)$$

where,  $p$  is the volume fraction of particles,  $K$  is the bulk modulus and  $\mu$  is the shear modulus. The subscripts (p) and (eff) denote particles and the composite, respectively, and

$$\varphi_{\text{eff}} = (\mu_{\text{eff}}/6)(9K_{\text{eff}} + 8\mu_{\text{eff}})/(K_{\text{eff}} + 2\mu_{\text{eff}}). \quad (5)$$

In the context of RCM, the D-EMT has to be applied sequentially for each inclusion material in a block of subcells. The volume fraction of each material in a block is determined by the number of subcells occupied by the material. The most compliant material is assumed to be the binder. The D-EMT approach is used to calculate the effective composite properties as each of the stiffer materials is sequentially added to the binder. The final effective property is assigned to the block of subcells and the process is repeated for the next level of recursion. It should be noted that the sequence of addition of materials can determine the final values of the effective properties of the composite. Also, any anisotropy in the distribution of particles in the RVE is ignored by the D-EMT approximation.

### 3.2. Finite element homogenization

An alternative to D-EMT homogenization is to use the finite element method (FEM) for direct numerical homogenization. In this section, we describe a FEM approach Bathe (1997) for calculating the effective elastic properties of blocks of subcells.

We use two-dimensional, plane strain, finite elements that avoid numerical integration to homogenize blocks of subcells. RSRG methods are quite sensitive to approximation errors (Renard et al., 2000). However, accurate FEM calculations for blocks of subcells with large modulus contrasts require considerable discretization of each subcell and hence involve large computational cost. Instead, we model each subcell using one nine-noded displacement based element (for particles), or one nine-noded mixed displacement/pressure based element (for the binder). Explicit forms of the strain–displacement and stress–strain relations are used to arrive at explicit forms for stiffness matrices (see Appendix A) and average stresses and strains in each element.

Periodic displacement boundary conditions are applied to each block of subcells (see Appendix B). The state of stress is calculated using FEM for an applied homogeneous normal or shear strain. The average stresses and strains in a block of subcells are then used to determine the effective stiffness matrix for the block using the relation

$$\int_V \sigma_{ij} dV = C_{ijkl}^{\text{eff}} \int_V \epsilon_{kl} dV, \quad (6)$$

where  $V$  is the volume of the block,  $C_{ijkl}^{\text{eff}}$  is the effective elastic stiffness tensor of the composite,  $\sigma_{ij}$  are the stresses, and  $\epsilon_{ij}$  are the strains.

The process is repeated after all the blocks at each level of recursion have been assigned effective stiffness matrices. The effective moduli of the RVE are calculated after the effective stiffness matrix has been determined for the final level of recursion. At this stage, the RVE is assumed to be isotropic and the following procedure is followed.

For the two-dimensional case, the effective stiffness matrix of the RVE is of the form

$$\mathbf{C} = \begin{bmatrix} C_{11}^{\text{eff}} & C_{12}^{\text{eff}} & 0 \\ C_{12}^{\text{eff}} & C_{22}^{\text{eff}} & 0 \\ 0 & 0 & C_{66}^{\text{eff}} \end{bmatrix}. \quad (7)$$

The approximate effective two-dimensional Young's modulus ( $E_{\text{eff}}^{\text{2D}}$ ) and Poisson's ratio ( $\nu_{\text{eff}}^{\text{2D}}$ ) are calculated using the relations

$$\nu_{\text{eff}}^{\text{2D}} = 2C_{12}^{\text{eff}} / (C_{11}^{\text{eff}} + C_{22}^{\text{eff}}); \quad E_{\text{eff}}^{\text{2D}} = 0.5(C_{11}^{\text{eff}} + C_{22}^{\text{eff}})[1 - (\nu_{\text{eff}}^{\text{2D}})^2]. \quad (8)$$

We assume that the composite is isotropic and that the two-dimensional properties to have been obtained from plane strain calculations. The three-dimensional Young's modulus ( $E_{\text{eff}}$ ), Poisson's ratio ( $\nu_{\text{eff}}$ ), and shear modulus ( $G_{\text{eff}}$ ) can then be calculated using the relations (Jun and Jasiuk, 1993)

$$v_{\text{eff}} = v_{\text{eff}}^{2D}/(1 + v_{\text{eff}}^{2D}); \quad E_{\text{eff}} = E_{\text{eff}}^{2D}[1 - (v_{\text{eff}})^2]; \quad G_{\text{eff}} = E_{\text{eff}}/[2(1 + v_{\text{eff}})]. \quad (9)$$

### 3.3. Generalized method of cells homogenization

The GMC (Paley and Aboudi, 1992) is another technique that has been used to calculate the effective properties of composites. When GMC is used as the homogenizer in RCM, a block of subcells is homogenized in a single step without explicit calculation of the stresses in the block. Thus, each block of subcells is considered to be a RVE in the GMC sense and periodic boundary conditions are applied implicitly to the block.

A brief description of the two-dimensional GMC follows. Fig. 3 shows a schematic of the RVE, the subcells and the notation (Aboudi, 1991) used in GMC. In the figure,  $(X_1, X_2)$  is the global coordinate system of the RVE and  $(x_1^{(\alpha)}, x_2^{(\beta)})$  is the local coordinate system of the subcell  $(\alpha\beta)$ .

It is assumed that the displacement function  $u_i^{(\alpha\beta)}$  varies linearly within a subcell  $(\alpha\beta)$  and can be written in the form

$$u_i^{(\alpha\beta)}(x_1^{(\alpha)}, x_2^{(\beta)}) = w_i^{(\alpha\beta)}(X_1, X_2) + \Phi_i^{(\alpha\beta)}x_1^{(\alpha)} + \Theta_i^{(\alpha\beta)}x_2^{(\beta)}, \quad (10)$$

where  $i$  represents the coordinate direction and takes the values 1 or 2, and  $w_i^{(\alpha\beta)}$  is the mean displacement at the center of the subcell  $(\alpha\beta)$ . The constants  $\Phi_i^{(\alpha\beta)}$  and  $\Theta_i^{(\alpha\beta)}$  represent gradients of displacement across the subcell. The strain–displacement relations for the subcell are given by

$$\epsilon_{ij}^{(\alpha\beta)} = \frac{1}{2} \left( \partial_i u_j^{(\alpha\beta)} + \partial_j u_i^{(\alpha\beta)} \right), \quad (11)$$

where  $\partial_1 = \partial/\partial x_1^{(\alpha)}$  and  $\partial_2 = \partial/\partial x_2^{(\beta)}$ .

If each subcell  $(\alpha\beta)$  has the same dimensions  $(2h, 2h)$ , then the average strain in the subcell can be obtained in terms of the displacement field variables using Eqs. (10) and (11), and

$$\langle \epsilon_{ij}^{(\alpha\beta)} \rangle_V = \frac{1}{4h^2} \int_{-h}^h \int_{-h}^h \epsilon_{ij}^{(\alpha\beta)} dx_1^{(\alpha)} dx_2^{(\beta)}. \quad (12)$$

We assume continuity of traction at the interface of two subcells. In addition, displacements and tractions are assumed to be periodic at the boundaries of the RVE. Applying the displacement continuity equations on an average basis over the interfaces between subcells, the average strain in the RVE can be expressed in terms of the subcell strains. The average subcell stresses can be obtained from the subcell

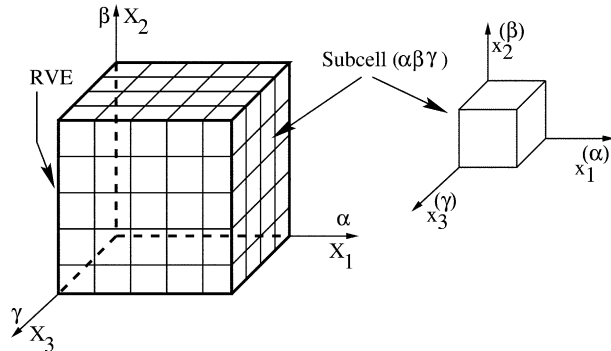


Fig. 3. RVE, subcells and notation used in GMC.

strains using the traction continuity condition and material stress–strain relations. A relationship between the subcell stresses and the average strains in the RVE is thus obtained.

For transversely isotropic or isotropic materials, the above approach leads to decoupled systems of equations for the normal and shear response of the RVE. The system of equations for the normal stresses and strains are of the form,

$$\begin{bmatrix} \mathbf{M}_{11} & \mathbf{M}_{12} \\ \mathbf{M}_{21} & \mathbf{M}_{22} \end{bmatrix} \begin{bmatrix} \mathbf{T}_1 \\ \mathbf{T}_2 \end{bmatrix} = \begin{bmatrix} \mathbf{H} \\ \mathbf{0} \end{bmatrix} \langle \epsilon_{11} \rangle_V + \begin{bmatrix} \mathbf{0} \\ \mathbf{H} \end{bmatrix} \langle \epsilon_{22} \rangle_V, \quad (13)$$

where  $\langle \cdot \rangle_V$  represents an average over the whole RVE.

The corresponding system of equations for the shear components are

$$\mathbf{M}_4 \mathbf{T}_{12} = \mathbf{H} \langle \epsilon_{12} \rangle_V. \quad (14)$$

In Eqs. (13) and (14) the  $\mathbf{M}$  matrices contain material compliance terms. The  $\mathbf{T}$  matrices contain the average subcell stresses. The vector  $\mathbf{H}$  contains the dimensions and number of subcells. After inverting these equations, explicit algebraic expressions are obtained relating the average RVE stresses to the average RVE strains. These equations are of the form

$$\begin{bmatrix} \langle \sigma_{11} \rangle_V \\ \langle \sigma_{22} \rangle_V \\ \langle \sigma_{12} \rangle_V \end{bmatrix} = \begin{bmatrix} C_{11}^{\text{eff}} & C_{12}^{\text{eff}} & 0 \\ C_{12}^{\text{eff}} & C_{22}^{\text{eff}} & 0 \\ 0 & 0 & C_{66}^{\text{eff}} \end{bmatrix} \begin{bmatrix} \langle \epsilon_{11} \rangle_V \\ \langle \epsilon_{22} \rangle_V \\ 2\langle \epsilon_{12} \rangle_V \end{bmatrix}, \quad (15)$$

where  $C_{ij}^{\text{eff}}$  are the terms of the effective stiffness matrix. Details of the algebraic expressions for these terms can be found elsewhere (Pindera and Bednarczyk, 1997).

Due to decoupling of the normal and shear response of the RVE, the shear components of the stiffness matrix obtained from GMC are the harmonic means of the subcell shear stiffnesses and of the form

$$1/C_{66}^{\text{eff}} = 1/N^2 \sum_{\alpha=1}^N \sum_{\beta=1}^N 1/C_{66}^{(\alpha\beta)}, \quad (16)$$

where  $N$  is the number of subcells per side of the RVE.

Once the stiffness matrix for a block of subcells has been calculated using GMC, the procedure is repeated recursively to get the effective stiffness of the RVE. The effective stiffness is then converted into moduli using the assumption of isotropy and Eqs. (8) and (9).

The shear modulus predicted by GMC is equal to the harmonic mean of the shear moduli of the subcells. This error can be ignored if the effective elastic properties of a particulate composite are computed from the normal components of the stiffness matrix.

#### 4. Polymer bonded explosives

PBXs are particulate composites containing a high volume fraction of explosive particles coated and supported by a binder. Some typical PBXs are shown in Table 1. It can be seen that the particle volume fraction in each of these materials is extremely high. The explosive particles are linear elastic at or below room temperature. The binder is viscoelastic at room temperature. The modulus contrast between particles and the binder is high, especially close to and above room temperature.

Table 1  
Typical polymer bonded explosives (Gibbs and Popolato, 1980)

PBX	Explosive particle		Binder	
	Material	Volume fraction	Material	Volume fraction
PBX 9010	RDX	0.87	KEL-F-3700	0.13
PBX 9501	HMX	0.92	Estane 5703 + BDNPA/F	0.08
PBX 9502	TATB	0.90	KEL-F-800	0.10

#### 4.1. Properties of PBX 9501 and constituents

PBX 9501 is a PBX containing monoclinic crystals of high melting explosive (HMX) dispersed in a viscoelastic binder which is a 1:1 mixture of a rubber (Estane 5703) and a plasticizer (bis dinitropropylacetal/formal—BDNPA/F). Since the HMX crystals are randomly oriented in PBX 9501, isotropic elastic properties can be used while modeling the particles in the composite.

Experiments on HMX (Zaug, 1998) show an average Young's modulus ( $E$ ) of 15.3 GPa and a Poisson's ratio ( $\nu$ ) of 0.32. Molecular dynamics simulations (Sewell and Menikoff, 1999) predict a Young's modulus of 17.7 GPa and a Poisson's ratio of 0.21 for HMX.

Experiments on the binder in PBX 9501 show temperature and strain rate dependence of elastic properties. The binder has a Young's modulus of approximately 0.7–1 MPa at low strain rates ( $\sim 0.001$ – $1$  s $^{-1}$ ) (Cady et al., 2000). The Young's modulus of HMX is around 20,000 times that of the binder at these strain rates. At high strain rates ( $\sim 1500$ – $3500$  s $^{-1}$ ), the Young's modulus of HMX is around 10–20 times that of the binder. The binder modulus decreases with increase in temperature. Since the binder is rubbery, it is assumed to have a Poisson's ratio of 0.49.

The Young's modulus of PBX 9501 at low strain rates is approximately 1 GPa, and at high strain rates around 5–7 GPa (Gray III et al., 1998). The Poisson's ratio of PBX 9501 is around 0.35 (Wetzel, 1999).

#### 4.2. Particle size distribution in PBX 9501

The dry blend of HMX particles in PBX 9501 is a mixture of two different size distributions of particles. The coarse HMX particles are sized between 44 and 300  $\mu$ m while the fine particles are less than 44  $\mu$ m. The particles are mixed in a 3 to 1 ratio of coarse to fine particles. In the composite, the smaller particles fit into the interstitial spaces between the larger ones.

The manufacture of PBX 9501 involves mixing the dry blend of HMX and the binder to form molding powder granules of PBX 9501. These powders are then isostatically compressed at 90 °C until the porosity is reduced to 1–2% and the pressed form of PBX 9501 is obtained. The size distribution of HMX particles in PBX 9501 after processing is significantly different from that before processing (Skidmore et al., 1997). The cumulative volume fraction of the finer sized particles is dramatically higher in pressed PBX 9501 compared to the dry blend. Fig. 4(a) shows the particle size distributions of HMX in the dry blend and the pressed piece. A sample microstructure of PBX 9501 is shown in Fig. 4(b).

#### 4.3. Bounds, analytical, and direct numerical estimates for PBX 9501

Table 2 shows third-order bounds and some analytical estimates for the effective bulk and shear moduli of PBX 9501 at low strain rate and room temperature. Rigorous third-order bounds (Milton, 1981) on the effective elastic properties of PBX 9501 at low strain rates can be observed to be considerably far apart. Commonly used analytical approximations such as the differential effective medium approximation (DEM)

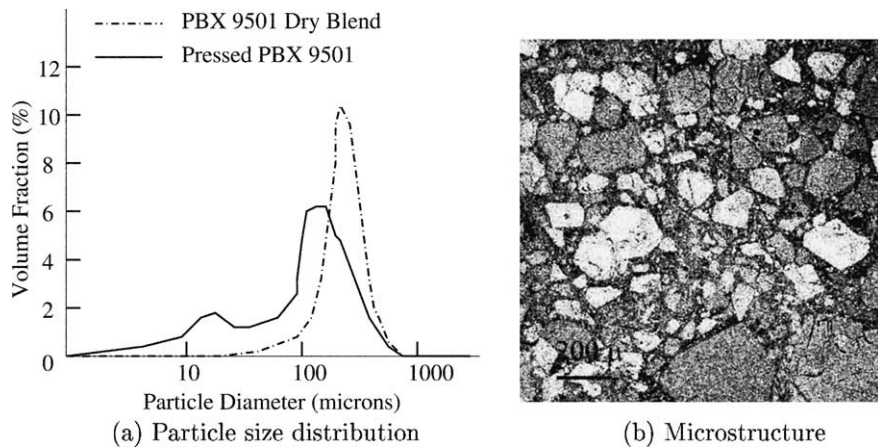


Fig. 4. Particle size distributions in the dry blend of PBX 9501 and in pressed PBX 9501 and the microstructure of PBX 9501 (adapted from Skidmore et al., 1997, 1998).

Table 2  
Bounds and analytical estimates of the effective elastic properties of PBX 9501

	Bulk modulus (MPa)	Shear modulus (MPa)
PBX 9501 (experiments)	1100	400
Third-order upper bound	11,300	5000
Third-order lower bound	220	70
Differential effective medium	230	80
Self-consistent scheme	11,050	4700

and the self-consistent scheme (SCS) (Markov, 2000) are also observed to provide inaccurate estimates for the elastic moduli of PBX 9501.

Direct numerical estimates of the effective elastic moduli of PBX 9501 have been discussed elsewhere (Banerjee, 2002). Direct finite element estimates have been found to require considerable computational expense because of the high degree of discretization required.

## 5. Estimates from the recursive cell method

In this section, estimates of effective moduli are obtained for RVEs containing 10–92% by volume of circular particles. These estimates show the performance of RCM both above and below the percolation threshold of  $\sim 0.80$ . Next, RCM is applied to models of PBX 9501 and the estimated moduli are compared with experimental data. Finally, some convergence properties of the method are explored and the strengths and weaknesses of the method are identified.

### 5.1. Models of random particulate composites

Fig. 5 shows two-dimensional RVEs of random composites containing circular particles. The volume fractions of particles vary from 0.10 to 0.92. The particle size distribution is roughly based on the particle size distribution of HMX in the dry blend of PBX 9501 (see Fig. 4(a)).

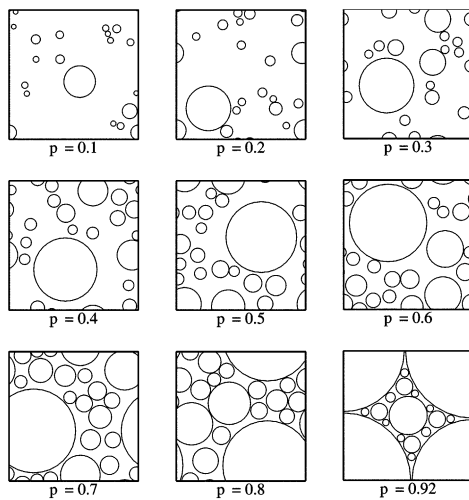


Fig. 5. RVEs containing 10–92% by volume of circular particles.  $p$  is the volume fraction of particles in a RVE.

A Young's modulus of 100 GPa and a Poisson's ratio of 0.20 were assigned to the particles. The Young's modulus of the binder was varied from 1 MPa to 10 GPa in multiples of 10 while the Poisson's ratio was kept fixed at 0.49.

The effective Young's moduli of these RVEs have been calculated using RCM with different homogenizers. For this purpose, each RVE was discretized into  $256 \times 256$  subcells. For the initial iteration, a subcell was assigned particle properties if it was found to contain >50% particles by volume. Otherwise the subcell was assigned binder properties. RCM estimates were obtained using blocks of  $2 \times 2$  and  $16 \times 16$  subcells, respectively.

To compare the RCM results with estimates from direct numerical simulations, plane strain finite element analyses were performed with each subcell being represented by a four-noded element. Periodic displacement boundary conditions were used to determine the average stresses and strains in the direct finite element computations. The effective moduli were calculated using the approach discussed in Section 3.2.

An extra set of calculation were performed with a binder Young's modulus 1 MPa so that convergence of the direct finite element calculations could be verified. In these direct FEM computations, each subcell of the RVE was modeled using a eight-noded quadrilateral element. Table 3 shows the values of effective modulus from four-noded and eight-noded computations. Eight-noded elements lead to lower effective moduli than four-noded elements. However, the difference is within 6% for volume fractions less than 0.80.

Table 3  
Comparison of effective Young's moduli from direct FEM calculations using four-noded and eight-noded elements

Volume fraction	0.10	0.20	0.30	0.40	0.50	0.60	0.70	0.79	0.92
Four-noded element (66 049 nodes)									
Modulus (MPa)	1.3	1.9	2.6	3.8	5.7	9.8	19.4	95.1	3542.3
Eight-noded element (197 633 nodes)									
Modulus (MPa)	1.3	1.8	2.6	3.7	5.4	9.4	18.3	89.2	2991.7
Difference (%)	0	5.3	0	2.6	5.3	4.1	5.7	6.2	15.5

The difference is 15.5% for the RVE containing 92% particles, primarily because the stress concentrations at particle contacts that dominate the calculation are not well resolved with four noded elements.

Fig. 6 shows the calculated effective Young's modulus of the nine RVEs as a function of volume fraction and modulus contrast. Note that the computed values at binder volume fractions of 0 and 1 are exact when computed using RCM (for all three homogenizers).

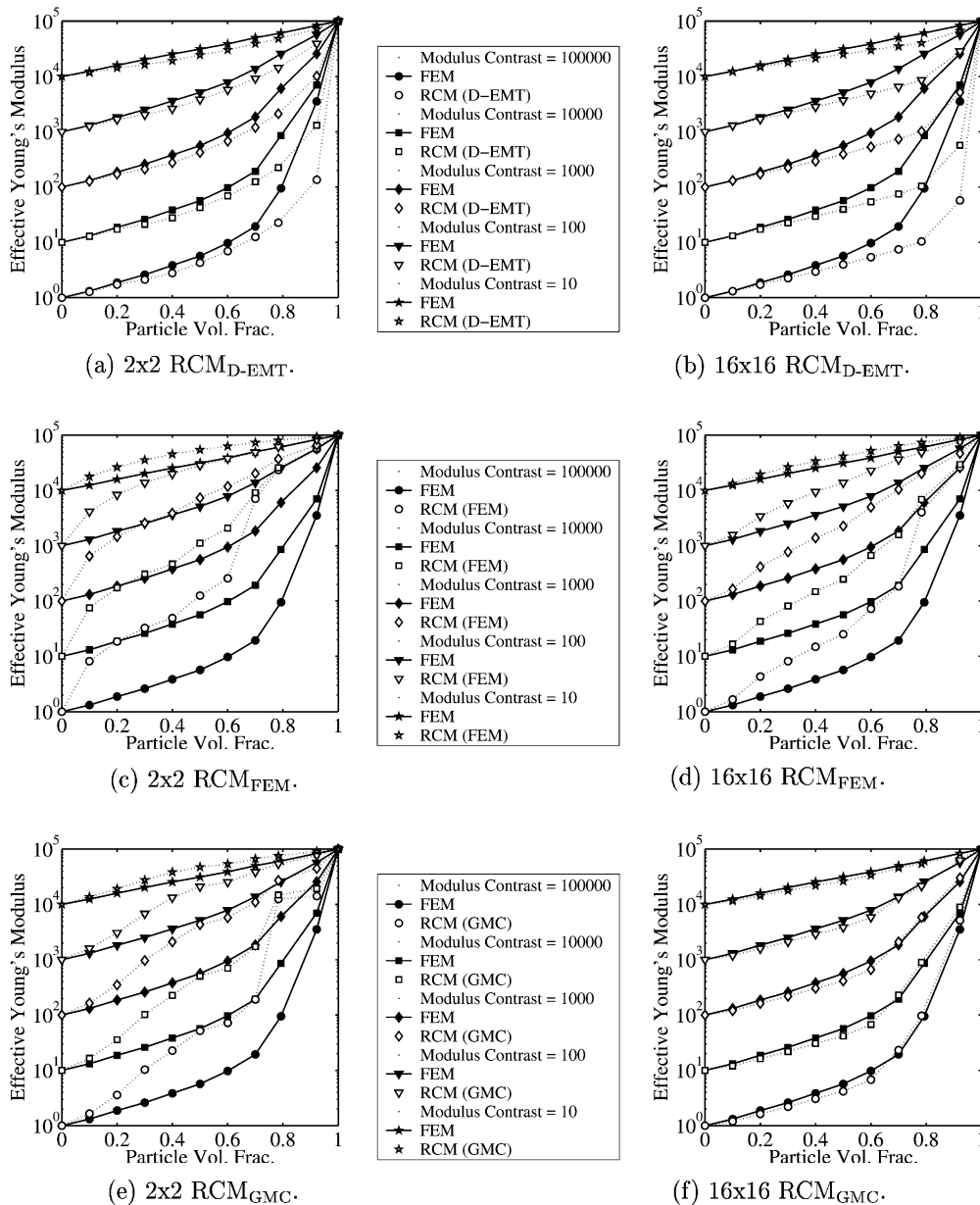


Fig. 6. Comparison of RCM and direct finite element estimates of effective Young's modulus for a range of modulus contrasts and volume fractions.

### 5.1.1. RCM with D-EMT homogenizer

The first set of RCM computations were performed using a D-EMT homogenizer ( $RCM_{D-EMT}$ ) as discussed in Section 3.1. Estimates using blocks of  $2 \times 2$  subcells are shown in Fig. 6(a). Those using blocks of  $16 \times 16$  subcells are shown in Fig. 6(b). The sequence of addition of materials in the D-EMT has been chosen to be in ascending order of Young's modulus. Use of other sequences leads to a difference of less than  $\pm 6\%$  in the estimated effective modulus of the microstructures considered.

From Fig. 6(a) it can be seen that the  $RCM_{D-EMT}$  calculations predict values that are less than the direct FEM estimates. Qualitatively, the difference is small for low particle volume fractions but is considerable for the volume fractions of 0.80 and 0.92. For example, for the volume fraction of 0.92 and binder modulus of 10 MPa, the  $RCM_{D-EMT}$  estimate is 1.3 GPa while the direct FEM estimate is 7 GPa. The difference grows larger when  $16 \times 16$  subcells are used to homogenize a block (as shown in Fig. 6(b)). In that case, the  $RCM_{D-EMT}$  estimate is 0.6 GPa. It should be noted that the  $RCM_{D-EMT}$  estimate is closer to the experimental value for PBX 9501 and may actually be the better estimate.

### 5.1.2. RCM with FEM homogenizer

The second set of RCM computations were performed using a FEM homogenizer ( $RCM_{FEM}$ ) as discussed in Section 3.2. Estimates using blocks of  $2 \times 2$  and  $16 \times 16$  subcells are shown in Fig. 6(c) and (d), respectively. The  $RCM_{FEM}$  estimates have been obtained from calculations in which each subcell in a block was modeled using a square, nine-noded, displacement based element.

The  $RCM_{FEM}$  estimates with  $2 \times 2$  subcells per block are almost an order of magnitude higher than the direct FEM estimates for all volume fractions and modulus contrasts shown in Fig. 6(c). When the number of subcells in a block is increased to  $16 \times 16$ , the estimates are closer to FEM predictions, especially for low modulus contrasts. These results suggest that further discretization of each block of subcells is required for  $RCM_{FEM}$  to predict moduli that are closer to direct FEM estimates.

### 5.1.3. RCM with GMC homogenizer

One of the reasons for the high  $RCM_{FEM}$  estimates is the low number of degrees of freedom in each block of subcells. However, increased discretization of a block of subcells decreases the computational efficiency of RCM. Since the GMC requires less discretization than finite elements for the same accuracy (Aboudi, 1996),  $RCM_{GMC}$  can be used for improved accuracy without significant loss of computational efficiency.

Since the displacement based FEM predicts elastic properties which are upper bounds (Banerjee, 2002), it is also possible that the overestimation of elastic properties by  $RCM_{FEM}$  is due to the accumulation of errors from both the FEM approximation and the renormalization technique. In this regard, since GMC predicts lower bounds on elastic properties (Banerjee, 2002), it is possible that predictions from  $RCM_{GMC}$  would improve over those from  $RCM_{FEM}$  because errors due to renormalization cancel out approximation errors in GMC.

The third set of RCM computations were performed using a GMC homogenizer ( $RCM_{GMC}$ ) as discussed in Section 3.3. Fig. 6(e) and (f) show the moduli from  $RCM_{GMC}$  calculations using blocks of  $2 \times 2$  and  $16 \times 16$  subcells, respectively.

The  $RCM_{GMC}$  estimates using blocks of  $2 \times 2$  subcells are closer to the FEM estimates of Young's modulus than the  $RCM_{FEM}$  results shown in Fig. 6(c). However, these estimates are considerably higher than the FEM and  $RCM_{D-EMT}$  predictions. When the subcells/block in a block is increased the  $RCM_{GMC}$  estimates improve. There are some pathological cases in which the error in the predicted modulus is higher than average (for the RVEs containing particle volume fractions of 0.50, 0.70 and 0.80). Considerably improved  $RCM_{GMC}$  estimates are obtained when  $16 \times 16$  subcells are used to form a block, as shown in Fig. 6(f). In that case, the  $RCM_{GMC}$  estimates are within a few percent of the direct FEM predictions for the RVEs.

It is interesting to note that the number of subcells per side (16), at which  $RCM_{GMC}$  provides good estimates, can be expressed as  $N^{1/d}$ , where  $N$  is the total number of subcells, and  $d$  is the dimensionality of the problem. Further exploration of this observation has not been carried out at this time.

#### 5.1.4. Computational expense

The direct FEM calculations on the RVEs (discretized into  $256 \times 256$  four-noded elements) using ANSYS 6.0 (ANSYS, 2002) take around 150 CPU seconds on a SunSparc Ultra-60 with 512 Mb RAM running Solaris 7. All the RCM programs were coded in Java using JDK 1.4. The  $16 \times 16$  subcells/block  $RCM_{D-EMT}$  calculations took around 10 CPU seconds to compute. The corresponding  $RCM_{FEM}$  calculations take around 130 CPU seconds, while  $RCM_{GMC}$  takes around 140 CPU seconds.

Thus, even the  $16 \times 16$  subcell  $RCM_{GMC}$  calculations provide a slight improvement in efficiency over direct finite element calculations. In addition, the  $16 \times 16$  subcell  $RCM_{GMC}$  provides a means of computing accurate effective properties for RVEs of high particle volume fraction particulate composites that need to be discretized considerably. In such cases, though direct finite element calculations may not be possible due to limitations on the available computational power, the effective properties of the RVE can be obtained using  $RCM_{GMC}$  calculations on smaller blocks of the whole RVE.

#### 5.2. Models of PBX 9501

A sample microstructure of PBX 9501 is shown in Fig. 4(b). The particles in the microstructure are irregularly shaped and of a large number of sizes. The volume fraction of particles in PBX 9501 is around 92%. A digital image of the microstructure is difficult to simulate since particles and binder are not easily distinguished. Instead, models containing circular particles with particle size distributions that correspond to that of PBX 9501 have been used to model the PBX.

The four microstructures shown in Fig. 7(a) are based on the particle size distribution of the dry blend of PBX 9501 (see Fig. 4(a)). The microstructures contain 100, 200, 300, and 400 particles, respectively. The corresponding RVE sizes are 0.65, 0.94, 1.13, and 1.325 mm. The particles in the microstructures occupy about 86% of the volume.

Microstructures based on the particle size distribution of pressed PBX 9501 are shown in Fig. 7(b). The four microstructures contain 100, 200, 500, and 1000 particles respectively. The corresponding RVE sizes are 0.36, 0.42, 0.535, and 0.68 mm. The particles occupy 89%, 87%, 86% and 85.5% of the volume, respectively. Higher volume fractions could not be achieved using the random sequential particle addition technique used. Also, particle sizes below 9  $\mu\text{m}$  have not been used because they fall below the resolution of the computational grid.

Since actual PBX 9501 contains 92% particles, the remainder of the particle volume fraction is incorporated into a 'dirty' binder. For example, the dirty binder in the models shown in Fig. 7(a) contains about 30% fine HMX particles and 70% binder. The D-EMT approach was used to determine the elastic properties of the dirty binder.

The model RVEs in Fig. 7 were discretized into  $256 \times 256$  subcells. Subcells containing more than 50% binder by volume were assigned dirty binder properties while those containing less than 50% binder were assigned particle properties. Note that this discretization and material assignment is also necessary for direct finite element computations since it is not possible to create elements of acceptable shape at the point of contact of two circular particles.

A Young's modulus of 15.3 GPa and a Poisson's ratio of 0.32 was used for the particles. These are the moduli of HMX at room temperature. The Young's modulus of the pure binder is 0.7 MPa and the Poisson's ratio is 0.49 at a temperature of 25  $^{\circ}\text{C}$  and a strain rate of 0.01  $\text{s}^{-1}$ . The elastic moduli of the dirty binder, using the HMX and pure binder properties above, for the models shown in Fig. 7(a) are 2.1 MPa (Young's modulus) and 0.48 (Poisson's ratio). For the four models in Fig. 7(b), the dirty binder moduli are

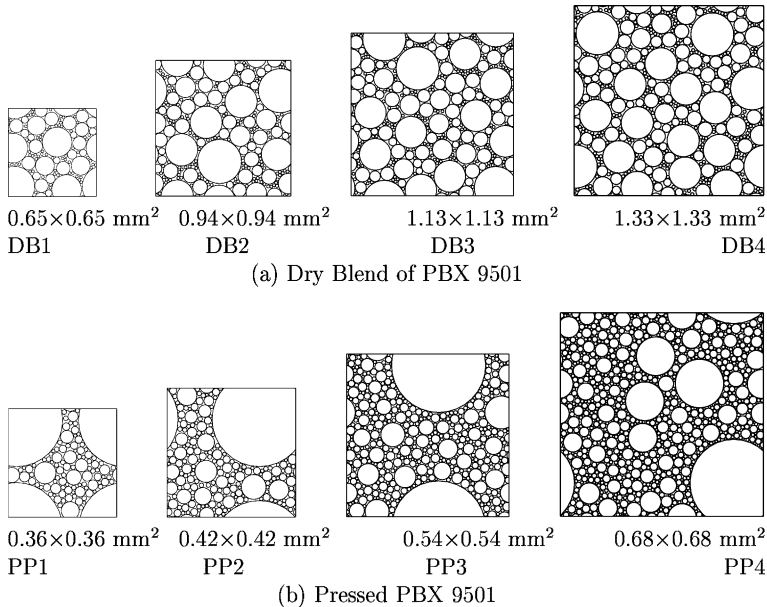


Fig. 7. Model microstructures representing PBX 9501. (a) Four microstructures based on the dry blend of PBX 9501. (b) Four microstructures based on the size distribution of pressed PBX 9501.

(1.6 MPa, 0.484) for model PP1, (2.1 MPa, 0.481) for model PP2, (2.7 MPa, 0.478) for model PP3, and (3.0 MPa, 0.477) for model PP4.

The effective moduli of the RVEs were calculated with RCM using 16×16 subcells/block. As a check, direct FEM estimates of the moduli were also obtained. These FEM calculations were performed by treating each subcell as an eight-noded element (197,633 nodes in the mesh). Table 4 shows the effective Young's moduli and Poisson's ratios of the models of PBX 9501 from RCM and direct FEM calculations. The ratio of the RCM estimates to the direct FEM estimates are also given as a measure of error, assuming that the direct FEM calculations are accurate.

For the models based on the dry blend, the  $RCM_{D-EMT}$  calculations predict Young's moduli that are less than 4% of the direct FEM estimates. This result can be expected based on the results shown in Fig. 6(b). The  $RCM_{FEM}$  estimates vary from 160% to 260% of the FEM values. This result also reflects the data for random particulates shown in Fig. 6(d). From the results shown in that figure, one should expect that, of the three homogenizers, the 16×16  $RCM_{GMC}$  calculations to provide the best estimates of the effective Young's modulus. However, this trend is not observed for the  $RCM_{GMC}$  estimates shown in Table 4.

From the table, it can be seen that the  $RCM_{GMC}$  estimates are between 7% and 15% of the FEM values, whereas the results in Fig. 6(f) show that GMC results are within 90% of the FEM values for the particulate RVEs considered. The same trends are observed from the data shown in Table 4 for the models of pressed PBX 9501. These results suggest that the effect of contact between particles is not being captured correctly by  $RCM_{GMC}$ , especially when such interactions dominate the material response.

### 5.2.1. Direct FEM computations

At this stage, it is of interest to check whether the direct FEM computations have converged to a stable value, whether the FEM predictions would decrease with further mesh refinement, and if the FEM predictions are close to the experimentally determined moduli of PBX 9501.

Table 4  
Effective moduli of PBX 9501

Model	Young's modulus (GPa)				Poisson's ratio			
	DB1	DB2	DB3	DB4	DB1	DB2	DB3	DB4
<i>Models of PBX 9501 dry blend</i>								
RCM <sub>D-EMT</sub>	0.05	0.06	0.10	0.09	0.40	0.38	0.37	0.37
RCM <sub>FEM</sub>	4.59	4.34	4.84	6.12	0.17	0.15	0.20	0.21
RCM <sub>GMC</sub>	0.12	0.32	0.16	0.42	0.32	0.19	0.29	0.15
Direct FEM	1.76	2.08	2.54	3.84	0.22	0.23	0.25	0.25
RCM <sub>D-EMT</sub> / FEM	0.03	0.03	0.04	0.02	1.8	1.7	1.5	1.5
RCM <sub>FEM</sub> / FEM	2.6	2.1	1.9	1.6	0.8	0.7	0.8	0.8
RCM <sub>GMC</sub> / FEM	0.07	0.15	0.06	0.11	1.4	0.8	1.2	0.6
 <i>Models of pressed PBX 9501</i>								
RCM <sub>D-EMT</sub>	0.07	0.10	0.14	0.15	0.38	0.36	0.35	0.34
RCM <sub>FEM</sub>	5.45	4.97	6.69	7.25	0.17	0.18	0.22	0.24
RCM <sub>GMC</sub>	0.13	0.23	0.24	0.20	0.33	0.22	0.21	0.26
Direct FEM	2.60	2.97	4.65	5.34	0.23	0.21	0.25	0.26
RCM <sub>D-EMT</sub> / FEM	0.03	0.03	0.03	0.03	1.7	1.7	1.4	1.3
RCM <sub>FEM</sub> / FEM	2.1	1.7	1.4	1.4	0.7	0.9	0.9	0.9
RCM <sub>GMC</sub> / FEM	0.05	0.08	0.05	0.04	1.4	1.05	0.8	1.0

Table 5 shows the results obtained from direct FEM computations for the eight model PBX 9501 microstructures. Errors with respect to a PBX 9501 Young's modulus of 1.0 GPa and a Poisson's ratio of 0.35 are also shown in the table.

The table shows that a threefold increase in the number of nodes leads, except in two cases, to a decrease of 10–15% in the effective Young's modulus. The Poisson's ratio does not appear to be affected significantly by mesh refinement. The effective Young's modulus does not always decrease with mesh refinement for the models of PBX 9501 unlike the models of random composites (see Table 3).

This discrepancy may indicate a lack of convergence of the FEM computations on the models of PBX 9501. It is conceivable that further refinement would lead to improved solutions. However, the associated computational cost is very high and further mesh refinement has not been explored except for one model (PP4). For model PP4, each subcell was subdivided into four eight-noded displacement elements (~800,000 nodes). FEM computations using this grid led to values of moduli that are only 3% lower than those using ~200,000 nodes. Hence, we may assume that the FEM computations have probably converged.

The use of generalized plane strain elements leads to lower values of Poisson's ratios indicating a stiffer lateral response than that using plane strain elements. The lower Young's moduli suggest a more compliant response in the direction of the applied strain. However, the difference between the plane strain and the generalized plane strain predictions is not large enough to warrant the extra computations required for the latter case.

Table 5  
Effective moduli of PBX 9501 from direct FEM calculations

Element	Nodes	Young's modulus (GPa)				Poisson's ratio			
		DB1	DB2	DB3	DB4	DB1	DB2	DB3	DB4
<i>Models of PBX 9501 dry blend</i>									
4-node (u)	66049	1.98	2.38	2.32	4.34	0.23	0.20	0.28	0.25
8-node (u)	197633	1.80	2.16	2.59	3.90	0.22	0.23	0.25	0.25
8-node (gu)	197633	1.78	2.09	2.56	3.82	0.21	0.22	0.24	0.23
8-node (u/p)	197633	1.76	2.08	2.54	3.84	0.22	0.23	0.25	0.25
4-node (u)	Error (%)	98	138	132	334	-34	-43	-20	-29
8-node (u)	Error (%)	80	116	159	290	-37	-34	-29	-29
8-node (gu)	Error (%)	78	109	156	282	-40	-37	-31	-34
8-node (u/p)	Error (%)	76	108	154	284	-37	-34	-29	-29
		PP1	PP2	PP3	PP4	PP1	PP2	PP3	PP4
<i>Models of pressed PBX 9501</i>									
4-node (u)	66049	2.93	2.79	5.24	6.16	0.23	0.24	0.25	0.26
8-node (u)	197633	2.66	3.02	4.70	5.39	0.23	0.21	0.25	0.26
8-node (u)	784841	—	—	—	5.17	—	—	—	0.26
8-node (gu)	197633	2.63	2.96	4.58	5.24	0.21	0.19	0.22	0.22
8-node (u/p)	197633	2.60	2.97	4.65	5.34	0.23	0.21	0.25	0.26
4-node (u)	Error (%)	193	179	424	516	-34	-31	-29	-26
8-node (u)	Error (%)	166	202	370	439	-34	-40	-29	-26
8-node (gu)	Error (%)	163	196	358	424	-40	-46	-37	-37
8-node (u/p)	Error (%)	160	197	365	434	-34	-40	-29	-26

Plane strain displacement elements are denoted by (u), plane strain displacement/pressure elements are denoted by (u/p), generalized plane strain displacement elements are denoted by (gu). Errors are given as percentages of the moduli of PBX 9501.

The mixed displacement/pressure elements provide the lowest values of effective Young's modulus. The error involved in using such elements, which are accurate for nearly incompressible materials, does not seem to be large enough to warrant their use either.

It is also observed that the models of PBX 9501 do not reflect the correct behavior of PBX 9501. The predicted Young's moduli of the dry blend models are between 70% and 300% higher than the moduli of PBX 9501. The comparisons are worse for the models of pressed PBX 9501—between 160% and 440% higher. There could be several possible causes for the discrepancy, some of which are listed below.

- (1) The materials model used for HMX, the binder, and/or PBX 9501 are incorrect. The effective elastic properties of thermoviscoelastic materials cannot be obtained without taking the loading history into consideration.
- (2) The use of circular particles is inappropriate. The actual shapes of the particles have to be modeled.
- (3) The dirty binder model is incorrect. The actual volume fraction of particles needs to be modeled.
- (4) The particle size distribution in the models is incorrect, especially after the RVE has been discretized and materials assigned using the 50% rule.
- (5) The use of a two-dimensional plane strain model leads to artificially high effective moduli.
- (6) A square RVE is inappropriate for the calculation of isotropic properties. RVEs with hexagonal symmetry should be used.
- (7) The RVEs are too small to represent PBX 9501. Larger RVEs with better discretization are needed.

The first two points and the sixth point above are the subject of ongoing investigations (Clements and Mas, 2001; Mas et al., 2003). The generation of models containing the correct volume fraction of particles and the right packing characteristics is extremely difficult, especially in three dimensions. Hence, a dirty binder, or a subgrid model that explicitly considers small scale interactions, is necessary. The effect of the dirty binder in our direct FEM computations is negligible. However, this need not be the case.

A possibility that is currently under investigation is to use two different homogenizations at the two length scales of HMX particle size in PBX 9501. In the first step, a binder containing around 70% HMX particles of 10–40  $\mu\text{m}$  size is homogenized. In the second step, the binder is replaced by the homogenized binder from the first step (dirty binder), HMX particles that are 100–400  $\mu\text{m}$  in size are added and a second homogenization is carried out. The particles are digitized from micrographs of PBX 9501 at the two length scales. Preliminary results from this study show that the exact cutoff between the two scales is not easy to determine and the predicted effective properties are strongly dependent on the volume fraction of particles in the second step of homogenization.

The particle size distribution in the RVEs prior to discretization is qualitatively close to the actual size distribution in PBX 9501 (dry blend or pressed). However, the peak of the size distribution of the dry blend is shifted to 275  $\mu\text{m}$  and there is a cutoff at 350  $\mu\text{m}$  (the size distribution of PBX 9501 is shown in Fig. 4(a)). For pressed PBX 9501, the peak for the larger particles is shifted to 150  $\mu\text{m}$  with an upper cutoff of 350  $\mu\text{m}$  while the peak for the smaller particles is shifted to 17  $\mu\text{m}$  with a cut off of 9  $\mu\text{m}$ . The particle distribution was sampled at around 10–20 points depending on the size of the RVE. Better matches to the distribution are obtained for the larger model RVEs which required more sampling to fill. However, better matches to the PBX 9501 particle size distributions could be obtained for larger RVEs and more frequent sampling.

It is true that the initial particle distributing changes dramatically after discretization and material assignment according to the 50% rule. The small particles are consolidated in one cell if the grid resolution is not high enough. In addition, extra contacts between particles can be generated which lead to increased stiffness. These errors can be reduced by increasing the number of cells in the grid. Direct FEM calculations using a grid of  $350 \times 350$  elements (Banerjee and Adams, in press) still predict values that are 2–4 times the experimental Young's moduli of PBX 9501. Comparisons of two- and three-dimensional direct FEM calculations on models of PBX 9501 (Banerjee, 2002) show that there is no significant difference between the predicted Young's moduli.

### 5.2.2. RCM with FEM homogenizer

In this section, we explore some possible causes of the high values of Young's modulus predicted by  $\text{RCM}_{\text{FEM}}$ . An example of a microstructure that leads to pathological behavior in RCM is also discussed, and compared with one of the models of PBX 9501 where particles are distributed randomly.

From Table 4, it can be seen that the values of Young's modulus predicted by  $\text{RCM}_{\text{FEM}}$  are 1.5–3 times the value obtained from direct FEM calculations. The Poisson's ratio are around 0.7–0.9 times the direct FEM estimates. Since nearly incompressible materials such as the binder can cause element locking (Bathe, 1997), the binder subcells were modeled with nine-noded mixed displacement–pressure elements. Use of these mixed elements was also observed not to cause any significant lowering of the estimated Young's modulus.

A possible source of error in the  $\text{RCM}_{\text{FEM}}$  estimates is that each subcell is modeled using only one element. An investigation has shown that if 1024 eight-noded elements are used to model a block of 256 subcells, the estimated effective Young's modulus is about 20% lower than that calculated using 256 elements. However, such high refinement is not allowable in the interest of computational efficiency and an alternative homogenization scheme may be the only option.

One of the requirements for a RSRG approach to work is that the total strain energy at each level of recursion is the same, i.e., the material is energetically equivalent for each representation. This issue is

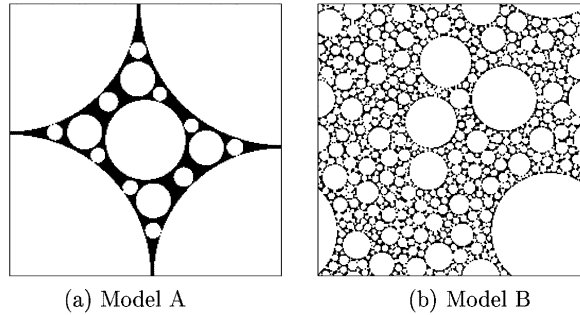


Fig. 8. (a) Manually generated microstructure with 92% by volume of particles with pathological behavior. (b) Automatically generated microstructure with 86% by volume of particles.

explored for RCM<sub>FEM</sub> using an example of a microstructure prone to pathological inaccuracy (Fig. 8(a)) and a microstructure with randomly distributed particles (Fig. 8(b)). Material properties of HMX and binder at room temperature and low strain rate were used for the RCM<sub>FEM</sub> computations on these microstructures. Each RVE was divided into  $256 \times 256$  subcells and materials were assigned according to the 50% rule.

Fig. 9(a) shows that the strain energy density of the RVE decreases with increase in the number of subcells per block. The data presented are for a uniform normal strain of 0.01 mm/mm. The data point in the figure that corresponds to 65536 subcells per block is from direct finite element calculations with  $256 \times 256$  four-noded elements. The strain energy density of each block of subcells was calculated using the relation

$$e = \frac{1}{2} \sum_1^N \boldsymbol{\sigma} : \boldsymbol{\epsilon}, \quad (17)$$

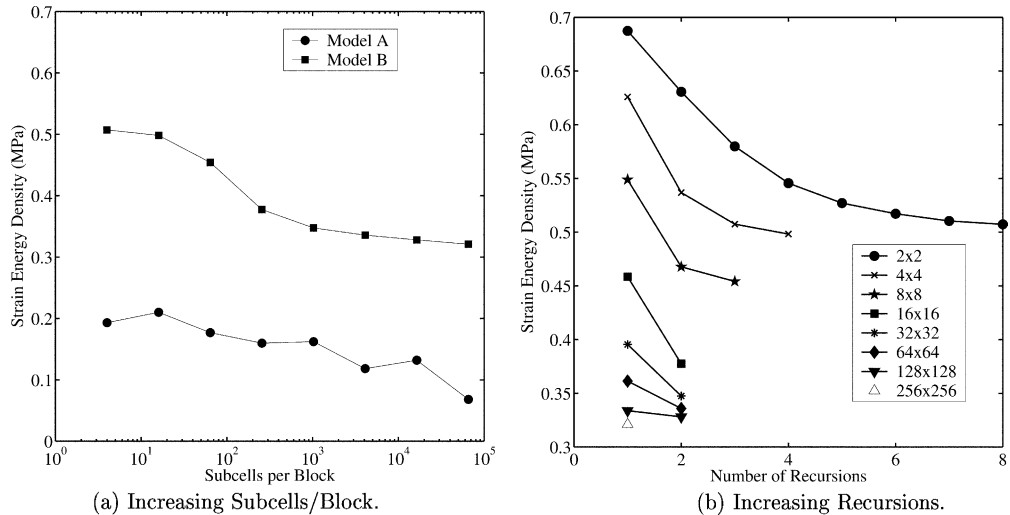


Fig. 9. (a) Variation of strain energy density of models A and B with increasing subcells/block. (b) Variation of strain energy density of model B with the number recursions and increasing subcells/block. The legend shows the number of subcells per block.

where  $e$  is the strain energy density of the block of subcells,  $N$  is the number of subcells in the block,  $\sigma$  is the volume averaged stress in a subcell,  $\epsilon$  is the volume averaged strain in a subcell, and  $:$  represents the tensor double contraction operation. The total strain energy density of the RVE was calculated by adding the strain energies of all the blocks.

For Model A the total strain energy from  $\text{RCM}_{\text{FEM}}$  calculations decreases by a factor of 2 with increasing subcells per block but remains around five times higher than the strain energy from the finite element calculation. The localization of the binder near the center of the subcell leads to the jumpy character of the strain energy density plot. This is a pathological problem with RCM. The results for Model B show that the particles are randomly distributed, a much better behavior is observed.

For Model B, the strain energy density starts at around 1.5 the finite element based value and converges rapidly toward that value. The random distribution of particles in the RVE contributes towards the smoothness of the convergence curve.

The fact that the strain energy density decreases with increasing subcells per block implies that the  $\text{RCM}_{\text{FEM}}$  results are necessarily inaccurate unless large blocks of subcells are homogenized at a time. The results also suggest that the larger the gap in the strain energy from  $2 \times 2$   $\text{RCM}_{\text{FEM}}$  calculations and the full FEM calculations, the slower the rate of convergence to an accurate estimate with increase in the number of subcells per block. However, this information cannot be utilized without a-priori knowledge of the finite element estimate.

From Fig. 9(b) it is observed that the strain energy density decreases with each recursion instead of remaining constant. This seriously undermines the applicability of a RSRG approach in the manner presented in this work. An improvement to RCM that would partially rectify this error would be to consider the effect of subcells in adjacent blocks instead of assuming periodicity of each block of subcells. Such an approach would decrease the difference in total strain energy density between different levels of recursion by making the material more compliant.

### 5.2.3. RCM with GMC homogenizer

The results shown in Table 4 show that  $\text{RCM}_{\text{GMC}}$  using  $16 \times 16$  subcells/block predict low values for the effective Young's modulus of models of PBX 9501. This error is caused by a known source of error in GMC—the underestimation of stress bridging (preferential stress paths due to particle–particle contact) (Banerjee, 2002). If stress is transported via particle–particle contact, the material exhibits a much stiffer behavior than if such paths do not exist. The underestimation of stress bridging leads the low values of Young's modulus in the  $\text{RCM}_{\text{GMC}}$  calculations of the PBX 9501 models. Since, the amount of stress bridging is lower or nonexistent in the models shown in Fig. 5, the  $16 \times 16$  GMC calculations predict much better estimates of effective properties.

The stress bridging issues can be partially circumvented using fewer subcells per block in  $\text{RCM}_{\text{GMC}}$ . In GMC, stress bridging due to particle–particle contact is not accurately accounted for unless there exist continuous particle paths (boundary to boundary) along rows or columns of subcells in a RVE. This problem can be avoided by using fewer subcells per block because the probability of the existence of such paths in small blocks of subcells is greater. In addition, errors due to the non-existence of such paths in certain blocks can be compensated for in other blocks.

Table 6 shows the results of  $\text{RCM}_{\text{GMC}}$  calculations for the eight models of PBX 9501 when smaller blocks of subcells are used. The  $\text{RCM}_{\text{GMC}}$  estimates of Young's modulus that are closest to the FEM estimates are obtained using  $4 \times 4$  subcells per block for the models of the dry blend and using  $2 \times 2$  subcells/block for the pressed PBX 9501 models. When more subcells are used to form a block, the error in the computation of stress bridging dominates and low values of effective Young's modulus are obtained. The  $\text{RCM}_{\text{GMC}}$  estimates of the effective Poisson's ratio are quite low except when  $16 \times 16$  subcells are used per block. This reflects the excessively stiff response of the RVE in the direction normal to the applied strain when two few subcells are used in a block.

Table 6  
Effective moduli of PBX 9501 from RCM<sub>GMC</sub> calculations

Subcells/block	Young's modulus (GPa)				Poisson's ratio			
	DB1	DB2	DB3	DB4	DB1	DB2	DB3	DB4
<i>Models of PBX 9501 dry blend</i>								
2×2	3.2	4.3	3.6	5.3	0.09	0.11	0.10	0.13
4×4	1.8	2.4	1.6	2.6	0.07	0.07	0.06	0.08
8×8	0.7	1.3	0.6	0.8	0.08	0.07	0.10	0.11
16×16	0.1	0.3	0.2	0.4	0.32	0.19	0.30	0.15
Direct FEM	1.8	2.1	2.5	3.8	0.22	0.23	0.25	0.25
	PP1	PP2	PP3	PP4	PP1	PP2	PP3	PP4
<i>Models of pressed PBX 9501</i>								
2×2	6.3	5.4	4.1	6.4	0.15	0.14	0.10	0.16
4×4	3.4	1.9	1.5	3.2	0.10	0.07	0.06	0.09
8×8	0.9	1.9	0.6	0.9	0.10	0.08	0.10	0.07
16×16	0.1	0.2	0.2	0.2	0.33	0.22	0.21	0.26
Direct FEM	2.6	3.0	4.7	5.3	0.23	0.21	0.25	0.26

The problem of inadequate stress bridging in GMC has been addressed by a recently developed version of GMC called the strain-compatible method of cells (SCMC) (Gan et al., 2000). If that technique works accurately, GMC can be replaced with SCMC as the homogenizer in RCM and blocks of 16×16 subcells could be used to compute the effective properties of a RVE. However, SCMC involves additional computational cost and has not been explored in this paper.

Overall, the RCM<sub>GMC</sub> approach appears to be an improvement over the RCM<sub>FEM</sub> approach for rapid estimation of the effective properties of PBX 9501 as well as for composites with lower volume fractions.

## 6. Summary and conclusions

Rigorous bounds and analytical approximations for the effective elastic properties of PBXs provide inaccurate estimates because of the high volume fraction of particles and the strong modulus contrast in these composites. Numerical approximations using the finite element method are computationally intensive for the same reasons. The RCM was developed so that effective elastic moduli of these composites could be obtained at low computational expense. A RSRG scheme forms the basis of the RCM.

Three homogenization schemes have been explored in the context of the RCM—the differential effective medium approach, the finite element method, and the GMC. The accuracy of the RCM has been explored by computing the effective properties of a set of microstructures containing circular particles occupying volume fractions from 0.10 to 0.92. Eight microstructures that represent PBX 9501 have been used to check the accuracy of the RCM when applied to PBXs. Direct finite element calculations have been used to determine the accuracy of the RCM.

When the differential effective medium approach is used as the homogenization tool, the predicted effective properties are found to be lower than finite element estimates. The error is considerable for high volume fractions of particles and tends to increase when the number of subcells in a block is increased.

For the homogenizer based on finite elements, estimates of effective Young's modulus are found to be considerably higher than predictions from direct finite element calculations. The error decreases with increase in the number of subcells in a block but continues to be large unless the number of subcells in a block is at least 1/4 the total number of subcells. It is possible that each block of subcells needs to be discretized

into more than one element per subcell for improved results. It is also observed that the improvement in the predicted elastic moduli depends strongly on the geometry of the microstructure being modeled. Better estimates are obtained if the particle distribution is random.

However, when the GMC is used as a homogenizer in the recursive cells method and blocks containing  $16 \times 16$  subcells are homogenized, the error in the estimates of effective elastic properties is quite small for models of random composites that have been investigated. This result suggests that the RCM, with a GMC homogenizer, can be used to calculate the effective elastic properties of random composites.

Unfortunately, the RCM is not very accurate for models of PBX 9501. The finite element homogenizer overestimates the effective properties while the GMC homogenizer considerably underestimates the effective properties. In addition, the direct finite element calculations tend to predict effective Young's moduli that are considerably higher than the experimentally observed moduli.

The low values predicted by the GMC homogenizer point to the fact that stress transfer through particle contact is not adequately modeled using the GMC. An improved version of the technique, such as the strain-compatible method of cells, could be used to obtain improved estimates. However, there is an accompanied increase in computational cost.

Though approaches such as the RCM can be considerably faster than direct numerical simulations, they are not recommended for high volume fraction and strong modulus contrast particulate composites such as PBX 9501. They can, however, be applied for more traditional particulate composite materials with particle volume fractions less than 0.80.

## Acknowledgements

This research was supported by the University of Utah Center for the Simulation of Accidental Fires and Explosions (C-SAFE), funded by the Department of Energy, Lawrence Livermore National Laboratory, under subcontract B341493. The authors would like to thank Prof. Graeme Milton for pointing out the similarity of the recursive cell method to other real-space renormalization group approaches. The authors would also like to thank the reviewers for their clarifying comments.

## Appendix A. Explicit element stiffness matrices

Explicit expressions for the stiffness matrix for nine-noded displacement based elements and a hybrid nine-noded displacement/pressure based element (for nearly incompressible behavior) are presented in this section. The explicit forms of the stiffness matrices eliminate the need for numerical integrations in the RCM calculations. A schematic of a nine-noded element is shown in Fig. 10.

### A.1. Displacement-based nine-noded element

The element stiffness matrix for the nine-noded displacement based element in Fig. 10 is shown in Table 7. This element can be used in conjunction with the nine-noded displacement/pressure based hybrid element. An orthotropic linear elastic material has been used to determine the element stiffness matrix. The stiffness matrix is, like that of the four noded element, independent of the location and size of the element.

### A.2. Mixed displacement–pressure nine-noded element

The binder used in PBXs is nearly incompressible and has a Poisson's ratio of about 0.49. The volumetric strain in the binder is therefore small under applied loads. In displacement based finite elements, the ele-

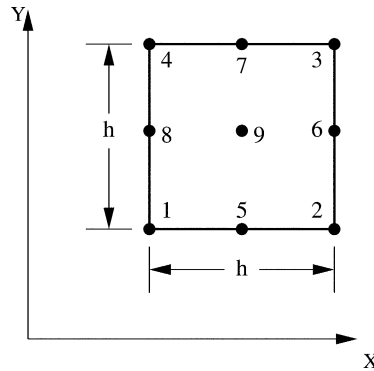
Fig. 10. Nine-noded finite element used in RCM<sub>FEM</sub> calculations.

Table 7  
Stiffness matrix for the displacement based nine-noded element

$j_2$	$j_5$	$e_2$	$-j_6$	.	.	.	$b_2$	$d_1$	$j_4$	$d_3$	$j_4$	$f_1$	$-b_2$	$-a_1$	$-b_1$
	$-j_1$	$-j_3$	$-e_4$	$j_6$	$-f_2$	.	$b_2$	$d_1$	$j_4$	.	.	.	.	.	.
$j_8$		$j_6$	$-h_4$	$-j_3$	.	.	.	.	.	.	.	.	.	.	.
		$-j_7$	$-j_6$	$h_2$	$-b_2$	$i_1$	$j_4$	$g_3$	$j_4$	$g_1$	$b_2$	$-i_2$	$-b_1$	$-c_1$	.
		$j_2$	$-j_5$	$-e_4$	$-j_6$	.	.	.	.	.	.	.	.	.	.
			$-j_1$	$j_3$	$-f_2$	$-b_2$	$f_1$	$b_2$	$d_3$	$-j_4$	$d_1$	$-j_4$	$-a_1$	$b_1$	.
			$j_8$	$j_6$	$h_2$	$j_3$	.	.	.	.	.	.	.	.	.
				$-j_7$	$b_2$	$i_1$	$-b_2$	$-i_2$	$-j_4$	$g_1$	$-j_4$	$g_3$	$b_1$	$-c_1$	.
.	$j_2$	$j_5$	$e_2$	$-j_6$	$d_3$	$j_4$	$f_1$	$-b_2$	$-f_2$	$b_2$	$d_1$	$j_4$	$-a_1$	$-b_1$	.
.		$j_8$	$j_6$	$-h_4$	$j_4$	$g_1$	$b_2$	$-i_2$	$-b_2$	$i_1$	$j_4$	$g_3$	$-b_1$	$-c_1$	.
.			$j_2$	$-j_5$	$d_3$	$-j_4$	$d_1$	$-j_4$	$-f_2$	$-b_2$	$f_1$	$b_2$	$-a_1$	$b_1$	.
.			$j_8$		$-j_4$	$g_1$	$-j_4$	$g_3$	$b_2$	$i_1$	$-b_2$	$-i_2$	$b_1$	$-c_1$	.
.				$e_1$	0	$-a_1$	$-b_1$	$-a_2$	0	$-a_1$	$b_1$	$d_2$	0	.	.
.					$h_3$	$-b_1$	$-c_1$	0	$c_2$	$b_1$	$-c_1$	0	$-d_4$	0	.
.						$e_3$	0	$-a_1$	$b_1$	$a_2$	0	.	.	.	.
.							$h_1$	$b_1$	$-c_1$	0	$-c_2$	0	$g_2$	.	.
.								$e_1$	0	$-a_1$	$-b_1$	$d_2$	0	.	.
.									$h_3$	$-b_1$	$-c_1$	0	$-g_4$	.	.
.	$s$	$y$	$m$	$m$	$e$	$t$	$r$	$y$			$e_3$	0	$-d_4$	0	.
.											$h_1$	0	$g_2$	.	.
.												$16a_1$	0	.	.
.													$16c_1$		.
$a_1 = \frac{8}{45}(C_{11} + C_{66})$	$a_2 = \frac{8}{45}(C_{11} - C_{66})$	$b_1 = \frac{4}{9}(C_{12} + C_{66})$	$b_2 = \frac{1}{3}(C_{12} - C_{66})$												
$c_1 = \frac{8}{45}(C_{22} + C_{66})$	$c_2 = \frac{8}{45}(C_{22} - C_{66})$	$d_1 = \frac{1}{45}(C_{11} + 4C_{66})$	$d_2 = \frac{16}{45}(C_{11} - 4C_{66})$												
$d_3 = \frac{8}{45}(4C_{11} + C_{66})$	$d_4 = \frac{16}{45}(4C_{11} - C_{66})$	$e_1 = \frac{8}{45}(4C_{11} + 7C_{66})$	$e_2 = \frac{1}{90}(4C_{11} - 7C_{66})$												
$e_3 = \frac{8}{45}(7C_{11} + 4C_{66})$	$e_4 = \frac{1}{45}(7C_{11} - 4C_{66})$	$f_1 = \frac{1}{45}(7C_{11} - 16C_{66})$	$f_2 = \frac{1}{45}(16C_{11} - 7C_{66})$												
$g_1 = \frac{8}{45}(C_{22} + 4C_{66})$	$g_2 = \frac{16}{45}(C_{22} - 4C_{66})$	$g_3 = \frac{8}{45}(4C_{22} + C_{66})$	$g_4 = \frac{16}{45}(4C_{22} - C_{66})$												
$h_1 = \frac{8}{45}(7C_{66} + 4C_{22})$	$h_2 = \frac{1}{90}(4C_{22} - 7C_{66})$	$h_3 = \frac{8}{45}(4C_{66} + 7C_{22})$	$h_4 = \frac{9}{90}(7C_{22} - 4C_{66})$												
$i_1 = \frac{1}{45}(7C_{22} - 16C_{66})$	$i_2 = \frac{1}{45}(16C_{22} - 7C_{66})$	$j_1 = \frac{a_1}{16}$	$j_2 = \frac{7a_1}{4}$												
$j_3 = \frac{b_1}{16}$	$j_4 = \frac{b_1}{4}$	$j_5 = \frac{9b_1}{16}$	$j_6 = \frac{b_2}{4}$												
$j_7 = \frac{c_1}{16}$	$j_8 = \frac{c_1}{4}$														

ment strain is determined from derivatives of displacements that are less accurately determined than nodal displacements. Therefore, errors in the predicted volumetric strain for nearly incompressible materials can lead to large errors in the predicted stresses. Since the external loads are balanced by the stresses, this also

implies that the predicted displacements will be inaccurate unless an extremely fine mesh is used. In practice, the displacements predicted by displacement based finite elements for nearly incompressible materials are much smaller than those expected (Bathe, 1997). This behavior is called element locking.

The nine-noded displacement/pressure element with three pressure degrees of freedom (also called a 9/3 u-p element) has been proven to avoid element locking (Bathe, 1997). This element is used for the RCM calculations on subcells containing the binder material. The 9/3 u-p element has the same geometry and node numbering scheme as that of the nine-noded element shown in Fig. 10(b). The stiffness matrix for this element is shown in Table 8 and is independent of size and location.

## Appendix B. Boundary conditions

The boundary conditions used to homogenize a block of subcells in RCM<sub>FEM</sub> are a uniform normal displacement in the  $x$  direction ('1' direction), a uniform normal displacement in the  $y$  direction ('2' direction), and a shear displacement in the  $xy$ -plane ('12' plane). The goal is to simulate unidirectional normal stress states and pure shear stress states so that the effective properties of a block of cells can be calculated from the effective stress-strain equations. The following discussion follows the approach taken by ANSYS 6.0 (ANSYS, 2002) in applying displacement boundary conditions.

The finite element problem involves the solution of a set of  $n$  linear equations relating the displacements  $u_j$  to the applied forces  $f_i$ . This system of equations can be written as

$$\sum_{j=1}^n K_{ij} u_j = f_i \quad (1 \leq i \leq n). \quad (\text{B.1})$$

The stiffness matrix is singular, and the set of equations can only be solved upon the application of suitable boundary conditions. The boundary conditions applicable for a block of four subcells are discussed below. Similar boundary conditions can be applied to a block of more than four subcells.

### B.1. Normal displacement

A schematic of a block of four subcells subjected to a normal displacement in the  $x$  direction is shown in Fig. 11. The figure shows the locations of the nodes in the original and deformed configurations. A uniform displacement  $\delta$  is applied to nodes 3, 6, 9 and node 1 is kept fixed. Nodes 2 and 3 are not allowed to move in the  $y$  direction. Similarly, nodes 4 and 7 are not allowed to move in the  $x$  direction. Nodes 7, 8 and 9 are constrained to move an equal amount in the  $y$  direction. The pair of nodes 2 and 8 are constrained so that they move an equal amount in the  $x$  direction while nodes 4 and 6 are constrained so that they move an equal amount in the  $y$  direction. The applied displacement  $\delta$  and the fixed displacements at nodes 1, 2, 3, 4 and 7 are called the prescribed displacements. The constrained displacements are described by constraint equations. In equation form, the prescribed displacements used in Fig. 11 are

$$u_1 = 0, \quad v_1 = 0, \quad v_2 = 0, \quad u_3 = \delta, \quad v_3 = 0, \quad u_4 = 0, \quad u_6 = \delta, \quad u_7 = 0, \quad u_9 = \delta,$$

and the constraint equations for this case are

$$u_8 - u_2 = 0, \quad v_6 - v_4 = 0, \quad v_8 - v_7 = 0, \quad v_9 - v_7 = 0,$$

where  $u$  and  $v$  are the nodal displacements in the  $x$  and  $y$  directions respectively and the subscript denotes the node number.

Similar boundary conditions apply for when a uniform displacement is applied in the  $y$  direction. The constraint equations are used to satisfy periodicity of displacements and may lead to stress states that are

Table 8  
Stiffness matrix for nine-noded mixed displacement/pressure element

$k_1$	$k_2$	$k_3$	$k_4$	.	.	.	.	.	.	.	.	.	.	.	.	.
$k_5$	$k_6$	$k_7$	$-k_4$	$k_8$	$k_9$	$-2k_7$	$k_{10}$	$k_{11}$	$k_{23}$	$k_{12}$	$k_{13}$	$k_{14}$	$-45$			
$k_1$	$-k_4$	$k_7$	$k_6$	.	.	.	.	.	.	.	.	.				
	$k_5$	$k_4$	$k_3$	$k_{13}$	$k_{12}$	$k_{23}$	$k_{11}$	$k_{10}$	$-2k_7$	$k_9$	$k_8$	$-45$	$k_{14}$			
$k_1$	$-k_2$	$k_7$	$k_4$	.	.	.	.	.	.	.	.					
	$k_5$	$-k_6$	$k_8$	$-k_9$	$k_{12}$	$-k_{13}$	$k_{11}$	$-k_{23}$	$-2k_7$	$-k_{10}$	$k_{14}$	$45$				
$k_1$	$-k_4$	$k_3$	$-k_6$	.	.	.	.	.	.	.						
	$k_5$	$-k_{13}$	$k_{12}$	$-k_9$	$k_8$	$-k_{10}$	$-2k_7$	$-k_{23}$	$k_{11}$	$45$	$k_{14}$	.				
$k_1$	$k_2$	$k_3$	$k_4$	.	.	.	.	.	.	.						
	$k_1$	$k_2$	$k_3$	$k_4$	.	.	.	.	.	.						
	$k_{11}$	$k_{23}$	$k_{12}$	$k_{13}$	$k_8$	$k_9$	$-2k_7$	$k_{10}$	$k_{14}$	$-45$						
.	$k_1$	$-k_4$	$k_7$	$k_{10}$	$-2k_7$	$k_9$	$k_8$	$k_{13}$	$k_{12}$	$k_{23}$	$k_{11}$	$-45$	$k_{14}$	.		
.	$k_1$	$-k_2$	$k_{11}$	$-k_{23}$	$-2k_7$	$-k_{10}$	$k_8$	$-k_9$	$k_{12}$	$-k_{13}$	$k_{14}$	$45$				
.	$k_1$	$-k_{10}$	$-2k_7$	$-k_{23}$	$k_{11}$	$-k_{13}$	$k_{12}$	$-k_9$	$k_8$	$45$	$k_{14}$	.				
.	$k_{15}$	0	$k_{14}$	$-k_{22}$	$k_{16}$	0	$k_{14}$	$k_{22}$	$k_{17}$	0						
.		$k_{18}$	$-45$	$k_{14}$	0	$k_{19}$	45	$k_{14}$	0	$k_{20}$	0					
.			$k_{18}$	0	$k_{14}$	45	$k_{19}$	0	$k_{16}$	0	$k_{17}$	.				
.				$k_{15}$	$k_{22}$	$k_{14}$	0	$k_{14}$	$-k_{22}$	$k_{17}$	0					
.					$k_{15}$	0	$k_{14}$	$-45$	$k_{14}$	0	$k_{20}$	.				
.						$k_{18}$	0	$k_{18}$	0	$k_{20}$	0					
.	$s$	$y$	$m$	$m$	$e$	$t$	$r$	$y$				$k_{15}$	0	$k_{17}$		
.												$k_{21}$	0			$k_{21}$
.																

$$A = \frac{4}{90}E/((1-2v)(1+v))$$

$$k_1 = 15 + \frac{137a}{2}$$

$$k_5 = \frac{75}{8} - \frac{23a}{4}$$

$$k_9 = \frac{135}{4} - \frac{135a}{2}$$

$$k_{13} = \frac{45}{4} + 60a$$

$$k_{17} = 60 - 116a$$

$$k_{21} = 240 + 592a$$

$$a = 1 - 2v,$$

$$k_2 = \frac{225}{16} + \frac{15a}{4}$$

$$k_6 = \frac{135}{16} - \frac{15a}{4}$$

$$k_{10} = \frac{45}{4} + \frac{15a}{2}$$

$$k_{14} = 30 - 32a$$

$$k_{18} = 105 + 205a$$

$$k_{22} = 15a$$

$$k_3 = \frac{15}{2} + \frac{5a}{8}$$

$$k_7 = \frac{15}{8} - \frac{43a}{8}$$

$$k_{11} = \frac{15}{2} + \frac{67a}{4}$$

$$k_{15} = 15 + 217a$$

$$k_{19} = 15 + a$$

$$k_{23} = \frac{45}{4}$$

$$k_4 = \frac{45}{16} + \frac{105a}{8}$$

$$k_8 = \frac{15}{2} - \frac{119a}{4}$$

$$k_{12} = \frac{105}{4} - \frac{95a}{4}$$

$$k_{16} = 15 - 11a$$

$$k_{20} = 120 - 116a$$

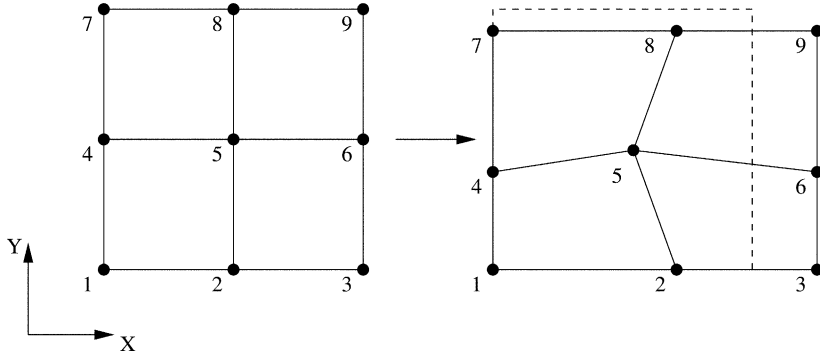


Fig. 11. Schematic of the effect of a uniform displacement applied in the  $x$  direction.

not purely unidirectional. However, for the materials under consideration, the deviations of the stresses from a unidirectional state of stress are small under the applied displacements.

### B.2. Shear displacement

The simulation of a state of pure shear is more problematic. Two schemes have been examined for this process and are shown in Fig. 12(a) and (b).

The scheme shown in Fig. 12(a) involves prescribing displacements that correspond to a pure shear at all the boundary nodes. In this approach, node 1 is fixed and node 9 is assigned displacements of magnitude  $\delta_1 + \delta_2$  in the  $x$  and  $y$  directions. Node 3 is assigned a displacement  $\delta_1$  in the  $x$  direction and a displacement  $\delta_2$  in the  $y$  direction. Similarly, node 7 has prescribed displacements of  $\delta_2$  in the  $x$  direction and  $\delta_1$  in the  $y$  direction. The nodes on the boundary that are between the corner nodes are assigned displacements such that the boundaries remain straight lines. The values of  $\delta_1$  and  $\delta_2$  are chosen so that they correspond to a pure shear displacement. Application of such boundary conditions leads to relatively high stresses in the  $x$  and  $y$  directions and a relatively stiff response.

An alternative to this approach of application of shear displacement boundary conditions is shown in Fig. 12(b). In this case, the displacements are prescribed only at the corner nodes while the other nodes on the boundary are constrained so that they maintain periodicity. Thus nodes 2 and 8 are constrained to have the same displacements in the  $x$  and  $y$  directions with node 8 being allowed an additional displacement corresponding to the shear displacement. A similar constraint equation relates the displacements at nodes 4 and 6. The normal stresses generated using this type of shear displacement boundary condition are much smaller than with the previous approach. However, when 9/3 u-p elements are used unrealistic displacements may be obtained at node 5 which do not occur when the first approach is used.

The prescribed shear displacements for the approach shown in Fig. 12(b) are

$$u_1 = 0, \quad v_1 = 0, \quad u_3 = \delta_1, \quad v_3 = \delta_2, \quad u_7 = \delta_2, \quad v_7 = \delta_1, \quad u_9 = \delta_1 + \delta_2, \quad v_9 = \delta_1 + \delta_2$$

and the corresponding constraint equations are

$$u_6 - u_4 = \delta_1, \quad v_6 - v_4 = \delta_2, \quad u_8 - u_2 = \delta_2, \quad v_8 - v_2 = \delta_1.$$

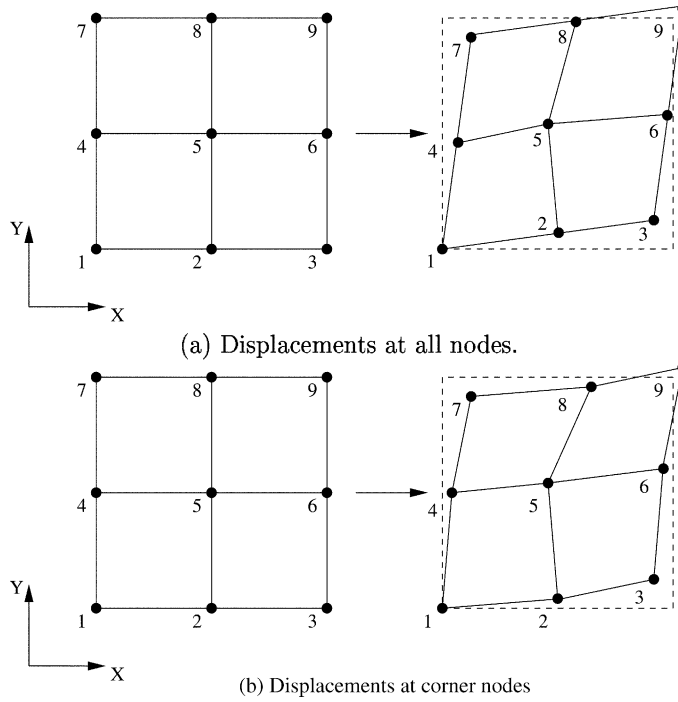


Fig. 12. Displacement boundary conditions corresponding to a pure shear. (a) Prescribed displacements are applied at all the boundary nodes. (b) Prescribed displacements are applied only at corner nodes.

### B.3. Application of constraint equations

An equation that relates the displacements of two nodes is called a constraint equation. For example, for the case shown in Fig. 11 a constraint equation is

$$u_2 - u_8 = 0,$$

where  $u_2$  is the displacement in the  $x$  direction at node 2 and  $u_8$  is the displacement in the  $x$  direction at node 8. In this case,  $u_2$  is the prime degree of freedom since it has a coefficient of +1. There can be many such constraint equations. In general form, these constraint equations can be written as,

$$\sum_{j=1}^n c_j u_j = C, \quad (B.2)$$

where  $C$  is a constant. If  $u_p$  is the prime degree of freedom then  $c_p = 1$ . For the RCM calculations, the condition  $c_p = 1$  is always satisfied.

Using the Lagrange multiplier technique, the original set of equations can be reduced by one to get a set of equations of the form:

$$\sum_{j=1}^n (K_{ij} - c_j K_{ip} - c_i K_{pj} + c_i c_j K_{pp}) u_j = f_i - CK_{ip} - c_i f_p + C c_i K_{pp} \quad (j \neq p). \quad (B.3)$$

Repeated application of this approach for each of the constraint equations gives us a set of equations with the redundant degrees of freedom removed. If there are  $n_c$  constraint equations, the reduced system of equations can be written as

$$\sum_{j=1}^{n-n_c} K_{ij} u_j = f_i \quad (1 \leq i \leq n - n_c). \quad (\text{B.4})$$

The specified displacements are used to further reduce the number of equations in the system shown in Eq. (B.4) in the usual manner before solving for the unknown displacements. At this stage, there are still some unknown nodal forces in the expressions for the force vector because of the constraint equations. These can be set to zero if we assume that the average forces are zero.

For the four subcell block subjected to a uniform normal displacement in the  $x$  direction (shown in Fig. 11), these nodal forces are

$$f_{x_2} + f_{x_8} = 0, \quad f_{y_4} + f_{y_6} = 0, \quad f_{x_5} = 0, \quad f_{y_5} = 0, \quad f_{y_7} + f_{y_8} + f_{y_9} = 0,$$

where  $f_x$  and  $f_y$  are the nodal forces in the  $x$  and  $y$  directions respectively. The subscripts 2, 4, 5, 6, 7, 8 and 9 refer to nodes at which the forces are applied. Similar equations are used when a uniform normal displacement is applied in the  $y$  direction. For displacements that correspond to a pure shear (shown in Fig. 12(b)), we again assume that the constrained nodal forces average to zero, i.e.,

$$f_{x_2} + f_{x_8} = 0, \quad f_{y_2} + f_{y_8} = 0, \quad f_{x_4} + f_{x_6} = 0, \quad f_{y_4} + f_{y_6} = 0, \quad f_{x_5} = 0, \quad f_{y_5} = 0.$$

Once the unknown forces have been accounted for using the above procedure, the system of equations can be solved for the unknown displacements.

## References

Aboudi, J., 1991. Mechanics of Composite Materials—A Unified Micromechanical Approach. Elsevier, Amsterdam.

Aboudi, J., 1996. Micromechanical analysis of composites by the method of cells—update. *Appl. Mech. Rev.* 49 (10), S83–S91.

ANSYS, 2002. ANSYS 6.0 User Manual. ANSYS Inc. [www.ansys.com](http://www.ansys.com).

Banerjee, B., 2002. Micromechanics-based prediction of thermoelastic properties of high energy materials. Ph.D. thesis, University of Utah, Salt Lake City, UT.

Banerjee, B., Adams, D., in press. Micromechanics-based prediction of effective elastic properties of polymer bonded explosives. *Physica B*.

Banerjee, B., Cady, C., Adams, D., 2003. Micromechanics simulations of glass-estane mock polymer bonded explosives. *Modelling Simul. Mater. Sci. Eng.* 11, 457–475.

Bardenhagen, S., Guilkey, J., Roessig, K., BrackBill, J., Witzel, W., Foster, J., 2001. An improved contact algorithm for the material point method and application to stress propagation in granular material. *Comput. Methods Eng. Sci.* 2 (4), 509–522.

Bathe, K.-J., 1997. Finite Element Procedures. Prentice-Hall, New York. p. 338–388.

Bernasconi, J., 1978. Real-space renormalization of bond disordered conductance lattices. *Phys. Rev. B* 18 (5), 2185–2191.

Cady, C., Blumenthal, W., Gray III, G., Idar, D., 2000. Mechanical properties of plastic-bonded explosive binder materials as a function of strain-rate and temperature. In: Proc. Intl. Conf. on Fund. Issues and Appl. of Shock-Wave and High-Strain-Rate Phenomena (EXPLOMET 2000), Albuquerque, NM.

Clements, B., Mas, E., 2001. Modeling high explosives with the method of cells and Mori-Tanaka effective medium theories. In: Proc., 12th APS Topical Conference on Shock Compression of Condensed Matter. American Physical Society, pp. 427–430.

Feng, S., Sahimi, M., 1985. Position-space renormalization for elastic percolation networks with bond-bending forces. *Phys. Rev. B* 31 (3), 1671–1673.

Gan, H., Orozco, C., Herakovich, C., 2000. A strain-compatible method for micromechanical analysis of multi-phase composites. *Int. J. Solids Struct.* 37, 5097–5122.

Garbozzi, E., Berryman, J., 2001. Elastic moduli of a material containing composite inclusions: Effective medium theory and finite element computations. *Mech. Mater.* 33 (8), 455–470.

Gell-Mann, M., Low, F., 1954. Quantum electrodynamics at small distances. *Phys. Rev.* 95 (5), 1300–1312.

Gibbs, T., Popolato, A., 1980. LASL Explosive Property Data. University of California Press, Berkeley, CA.

Gray III, G., Idar, D., Blumenthal, W., Cady, C., Peterson, P., 1998. High- and low-strain rate compression properties of several energetic material composites as a function of strain rate and temperature. In: Proc. 11th International Detonation Symposium, Snowmass, CO, pp. 76–84.

Hristopulos, D., Christakos, G., 1999. Renormalization group analysis of permeability upscaling. *Environ. Res. and Risk Assess.* 13, 131–160.

Jaekel, U., Vereecken, H., 1997. Renormalization group analysis of macrodispersion in a directed random flow. *Water Resour. Res.* 33 (10), 2287–2299.

Jun, S., Jasiuk, I., 1993. Elastic moduli of two-dimensional composites with sliding inclusions—a comparison of effective medium theories. *Int. J. Solids Struct.* 30 (18), 2501–2523.

King, P., 1989. The use of renormalization for calculating effective permeability. *Transport Porous Media* 4, 37–58.

Markov, K., 2000. Elementary micromechanics of heterogeneous media. In: Markov, K., Preziosi, L. (Eds.), *Heterogeneous Media: Micromechanics Modeling Methods and Simulations*. Birkhauser, Boston, pp. 1–162.

Mas, E., Clements, B., Schlei, B., 2003. Applying image analysis information into models and simulations of the mechanical response of PBX 9501. In: Proc. 13th APS Topical Conference on Shock Compression of Condensed Matter. American Physical Society, Portland, OR.

Milton, G., 1981. Bounds on the electromagnetic, elastic and other properties of two-component composites. *Phys. Rev. Lett.* 46 (8), 542–545.

Paley, M., Aboudi, J., 1992. Micromechanical analysis of composites by the generalized cells model. *Mech. Mater.* 14, 127–139.

Pindera, M.-J., Bednarcyk, B.A., 1997. An efficient implementation of the GMC micromechanics model for multi-phased materials with complex microstructures. *Tech. Rep. NASA-CR 202350*, National Aeronautics and Space Administration, Lewis Research Center, USA.

Poutet, J., Manzoni, D., Hage-Chehade, F., Jacquin, C., Boutea, M., Thovert, J.-F., Adler, P., 1996. The effective mechanical properties of random porous media. *J. Mech. Phys. Solids* 44 (10), 1587–1620.

Renard, P., Le Loch, G., Ledoux, E., de Marsily, G., Mackay, R., 2000. A fast algorithm for the estimation of equivalent hydraulic conductivity of heterogeneous media. *Water Resour. Res.* 36 (12), 3567–3580.

Sewell, T., Menikoff, R., 1999. Elastic coefficients and sound speeds for HMX polymorphs from molecular dynamics simulations, personal communication.

Shah, N., Ottino, J., 1986. Effective transport properties of disordered multi-phase composites: application of real-space renormalization group theory. *Chem. Eng. Sci.* 41 (2), 283–296.

Skidmore, C., Phillips, D., Son, S., Asay, B., 1997. Characterization of HMX particles in PBX 9501. In: Proc. 10th APS Topical Conference on Shock Compression of Condensed Matter. American Physical Society, Los Alamos, NM, pp. 112–119.

Skidmore, C., Phillips, D., Howe, P., Mang, J., Romero, J., 1998. The evolution of microstructural changes in pressed HMX explosives. In: Proc. 11th International Detonation Symposium, Snowmass, CO, pp. 556–564.

Stauffer, D., Aharony, A., 1992. *Introduction to Percolation Theory*, second ed. Taylor and Francis, London.

Stueckelberg, E., Petermann, A., 1953. La normalisation des constantes dans la theorie des quanta. *Helv. Phys. Acta* 26, 499–521.

Wetzel, B., 1999. Investigation of the creep behavior of nonlinear viscoelastic simulant materials for high explosives. Master's thesis, California Institute of Technology, Pasadena, CA.

Wilson, K., 1971a. Renormalization group and critical phenomena. I. Renormalization group and Kadanoff scaling picture. *Phys. Rev. B* 4 (9), 3174–3183.

Wilson, K., 1971b. Renormalization group and strong interactions. *Phys. Rev. D* 3 (8), 1818–1846.

Wilson, K., 1979. Problems in physics with many scales of length. *Scientific American* 241 (August), 158–179.

Zaug, J., 1998. Elastic constants of  $\beta$ -HMX and tantalum, equations of state of supercritical fluids and fluid mixtures and thermal transport determinations. In: Proc., 11th International Detonation Symposium, Snowmass, CO, pp. 498–509.